

**Mechanism of Methanol Synthesis on Ni(110)**

Journal:	<i>Catalysis Science & Technology</i>
Manuscript ID	CY-ART-01-2021-000107.R2
Article Type:	Paper
Date Submitted by the Author:	17-Mar-2021
Complete List of Authors:	Peng, Guowen; University of Wisconsin - Madison, Chemical and Biological Engineering Xu, Lang; University of Wisconsin-Madison, Department of Chemical and Biological Engineering; Glezakou, Vanda; Pacific Northwest National Laboratory, PCSD Mavrikakis, Manos; University of Wisconsin Madison, Chemical and Biological Engineering

Mechanism of Methanol Synthesis on Ni(110)

Guowen Peng^{1‡}, Lang Xu^{1‡}, Vassiliki-Alexandra Glezakou², and Manos Mavrikakis^{1*}

¹Department of Chemical and Biological Engineering, University of Wisconsin-Madison, Madison, Wisconsin 53706

²Chemical and Materials Sciences Division, Pacific Northwest National Laboratory, Richland, WA 99352

*E-mail: manos@engr.wisc.edu

‡These authors contributed equally.

Abstract: Planewave density functional theory (DFT-PW91) calculations are employed to study the methanol synthesis through CO₂ and CO hydrogenation, as well as the two side reactions: the water gas shift (WGS) reaction and the formic acid formation, on Ni(110). For the WGS reaction on Ni(110), we find that the redox mechanism is favored over the carboxyl-mediated mechanism. We show that the formate pathway is the dominant one for formic acid formation. For methanol synthesis through CO₂ and CO hydrogenation on Ni(110), our results reveal that the formic-acid- and dioxymethylene-mediated pathways coexist, in contrast to methanol synthesis on Cu(111) where the formic-acid-mediated pathway dominates. We also find that on Ni(110), hydrogenation of CH₂O* to CH₃O* and that to CH₂OH* both contribute to MeOH

synthesis. Based on the derived energetics, we ascertain that CH_3O^* hydrogenation to CH_3OH^* is likely the rate-determining step along the CH_3O^* pathway on Ni(110). Remarkably, CH_3O^* hydrogenation can be facilitated by the presence of HCO^* , demonstrating the promotional effect of CO. We further show that CO also participates in methanol synthesis directly via its hydrogenation to HCO^* and further to CH_2O^* . Additional microkinetic modeling by considering feed composition and reaction conditions would provide further mechanistic insights into methanol synthesis on Ni(110).

Keywords: methanol synthesis, water-gas-shift, formic acid, density functional theory, nickel catalyst, reaction mechanism.

1. Introduction

Carbon capture and sequestration is of prominent importance due to the overwhelming scientific evidence that CO_2 emissions have caused major climate changes. Direct utilization of CO_2 as a raw material to synthesize useful chemicals, such as methanol (CH_3OH) or formic acid (HCOOH), is thus of great interest for practical processes.^{1,2} On one hand, CO_2 is an abundant carbon source. On the other hand, the removal of CO_2 from industrial emissions can reduce its greenhouse effect.

Methanol is an alternative energy carrier and can be used as a transportation fuel³ in either modified internal combustion engines or direct methanol fuel cells.^{4,5} Methanol is currently synthesized in industry from a mixture of CO₂, CO, and H₂ over Cu/ZnO/Al₂O₃ catalysts.⁶ Much experimental and theoretical work has been done on methanol synthesis over Cu catalysts.⁷⁻³⁴ There is still a debate on the main carbon source (CO₂ or CO) for methanol synthesis. It is generally accepted that the CO₂ hydrogenation path plays the major role,^{11,12,18} though Yang et al. reported a shift of primary carbon source from CO₂ to CO at low reaction temperature.²² In an effort to explain experimental reaction kinetics data for MeOH synthesis over supported Cu/ZnO/Al₂O₃ catalysts, Grabow and Mavrikakis studied methanol synthesis on Cu(111) using density functional theory (DFT) calculations combined with a detailed mean-field microkinetic model.³⁵ They concluded that under the typical industrial methanol synthesis conditions, CO₂ hydrogenation contributes approximately 2/3 of the methanol produced while CO hydrogenation contributes the rest. A formic-acid-mediated pathway was found to be dominant for methanol synthesis on these Cu catalysts. It was proposed that CO is not only a promoter, but also a participant of methanol synthesis on Cu. A similar reaction pathway has been proposed on pure and Zn-modified Cu(211) stepped surfaces.^{19,23,24}

Interestingly, it has been reported that on a Ni-modified Cu(001) model surface, the rate of methanol formation is significantly increased, with a turnover frequency on a Ni site ~ 60 times higher than that on a Cu site.^{36,37} This has been tentatively ascribed to a promotional effect by CO which leads to Ni segregation to the surface. More recently, Alharthi and coworkers synthesized zeolite-supported Cu-Ni alloys catalysts with varying composition and demonstrated the highest methanol synthesis activity with a Cu-to-Ni molar ratio of 2.³⁸ Tan et al. also synthesized a Cu₁Ni₂ catalyst supported on CeO₂ nanotubes with enhanced methanol synthesis activities over pure Cu catalysts.³⁹ The potential for enhanced methanol synthesis activity is particularly attractive for industrial applications, as it offers a means to reduce the operating temperature (currently ~250 °C on industrial Cu/ZnO/Al₂O₃ catalysts), thus lowering the energy cost for the process. A lower reaction temperature is also desired if a Ni-containing catalyst is used for methanol synthesis, as Ni is known to also catalyze the methanation reaction for CO and CO₂ at around 250 °C.⁴⁰⁻⁴² Selective production of methanol on Ni therefore requires operating at a sufficiently low temperature to avoid activation of the O—C bond in CO/CO₂ which eventually leads to methane formation.

Insights into the reaction mechanism of CO₂ and CO hydrogenation to methanol over model Ni surfaces could provide insights on the role of Ni in methanol synthesis. Among the low-Miller-

index facets of Ni (Ni(111), Ni(100), and Ni(110)), Wang and co-workers demonstrated using DFT calculations that CO₂ binds the strongest to Ni(110).⁴³ Various experimental studies also evidenced the existence of stable CO₂ adsorption structures on Ni(110) under ultrahigh vacuum (UHV) conditions.^{44,45} Vesselli et al. observed hydrogenation of CO₂ to formate (HCOO) on Ni(110) under UHV conditions.⁴⁶ These findings suggest that Ni(110) is a promising model surface for the study of methanol synthesis.

Here, we systematically study methanol synthesis on Ni(110) through CO₂ and CO hydrogenation using planewave density functional theory calculations. We consider all possible elementary steps for the WGS reaction, formic acid formation, and methanol synthesis from CO₂ and CO hydrogenation. We first discuss the WGS reaction and compare the redox and carboxyl-mediated mechanisms. We then investigate formic acid formation via the formate and carboxyl pathways. After that, we systematically study methanol synthesis via CO₂ hydrogenation along the formic-acid- and dioxymethylene-mediated pathways. Since our main focus is to explore the conversion of CO₂ and CO to methanol, potentially at temperatures lower than the typical methanation temperature on Ni catalysts, we did not include any steps involved in the CO/CO₂ methanation reaction, which has been otherwise extensively studied in the literature.^{40-42,47-50} Importantly, the role of CO as either a reactant in or a promoter of methanol synthesis is

examined in detail. Based on our DFT data, we construct the reaction network for the WGS reaction, formic acid formation, and methanol synthesis on Ni(110).

2. Computational Methods

All calculations were performed using the Vienna ab-initio Simulation Package (VASP) code^{51,52}. The projector augmented-wave (PAW) potentials^{53,54} were used for electron-ion interactions, and the generalized gradient approximation (GGA-PW91)⁵⁵ was used to describe the exchange-correlation functional. The Ni(110) surface was modeled by a (2×3) surface unit cell in a seven-layer slab, separated from its successive images in the *z*-direction by a vacuum region ~12 Å thick. Adsorption is allowed on only one side of the metal slab, and the electrostatic potential was adjusted accordingly. The slab geometry and the high-symmetry sites on the slab are illustrated in Figure 1.^{56,57} The electron wave function was expanded using plane waves with an energy cutoff of 400 eV. The Brillouin zone was sampled with a (4×4×1) *k*-point mesh based on the Monkhorst-Pack scheme.⁵⁸ The climbing-image nudged elastic band (CI-NEB) method⁵⁹ was used to calculate the activation energy barrier and the reaction coordinate for each elementary step considered. Seven intermediate images were interpolated between the initial and final structures for each CI-NEB calculation. The three bottom-most Ni(110) layers were

fixed during energy minimization; all other layers and the adsorbates were allowed to relax. Structures were fully relaxed until the Hellmann-Feynman forces acting on the atoms were smaller than 0.05 eV/Å. Transition states were verified by identifying a single imaginary frequency. The binding energy is defined as $BE = E_{\text{ads}} - E_{\text{clean}} - E_{\text{gas}}$, where E_{ads} , E_{clean} , and E_{gas} are the calculated total energies of the slab with adsorbate, the clean slab, and the adsorbate species in the gas phase, respectively. All calculations were performed spin-polarized; the ferromagnetic phase was adopted for Ni(110). The calculated Ni lattice constant is 3.52 Å, in good agreement with the experimental value of 3.524 Å.⁶⁰

The vibrational frequencies ν_k and normal coordinates q_k were determined by diagonalizing the Hessian matrix which was evaluated by displacing the atoms in x , y , and z directions by ± 0.015 Å. The first-order infrared intensity of the k th normal mode was estimated by calculating the first derivative of the z -component of the dynamic dipole moments μ_z with respect to the normal mode q_k according to the formula⁶¹

$$I_k \propto \left| \frac{d\mu_z}{dq_k} \right|^2.$$

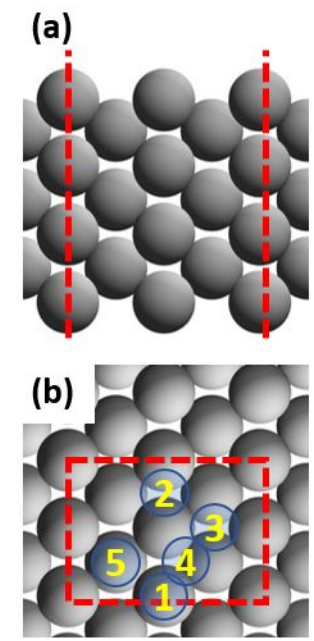


Figure 1. (a) Cross-section and (b) top views of the Ni(110) slab used in this study. The red dash lines indicate the (2x3) unit cell. The high-symmetry sites are marked on the top view: 1 – top; 2 – short-bridge (SB); 3 – long-bridge (LB); 4 – pseudo three-fold (PT); and 5 – hollow (HL).

3. Results and Discussion

3.1. Structure and Energetics of Adsorbed Intermediates

We first studied the adsorption of all relevant intermediate species on Ni(110). Shown in Figures 2(a) – (v) are top and cross-section views of the atomic structures of the most favorable adsorbed states for the 22 intermediate species. The preferred adsorption site and the respective binding energies are summarized in Table 1. The calculated vibrational frequencies are listed in Table S1, where the calculated frequencies of gas-phase H_2 , CO , CO_2 , H_2O , CH_2O , HCOOH , CH_3OH , and HCOOCH_3 are also included.

H, O, OH, H₂O, CO, and CO₂. The calculated binding energies for H at PT (Figure 2a) and SB sites are very close to each other, -2.74 and -2.71 eV, respectively. LB, HL, and top sites are less stable, with calculated binding energies of -2.66, -2.51, and -2.44 eV, respectively. The binding of H on Ni(110) is slightly weaker than that calculated on Ni(111) at 1/9 ML overage (BE = -2.83 eV).⁶² Oxygen also prefers the PT site with a binding energy of -5.30 eV (Figure 2b), 0.08 eV more stable than that at the SB site. OH binds to the surface through the oxygen atom; the SB site is the most favorable with a binding energy of -3.67 eV (Figure 2c). We note that at the SB site, OH is tilted away from the surface normal by an angle of 63°. H₂O prefers to bind to the top site via its O with a binding energy of -0.46 eV (Figure 2d). H₂O binding at the LB and HL sites is very weak with a calculated binding energy of -0.11 and -0.03 eV, respectively; the PT and SB sites are unstable. CO binds through its C atom with the molecule standing perpendicular to the surface. For CO adsorption, the most favorable binding site is the SB site with a binding energy of -1.92 eV (Figure 2e), which is approximately equal to the calculated binding energy of CO on Ni(111) at CO coverage of 1/3 monolayer.⁶³ The calculated binding energies of CO at PT, top, and LB sites are -1.77, -1.75, and -1.56 eV, respectively. For CO₂ adsorption, the V-shaped CO₂^{δ-} configuration is the most stable (Figure 2f), with a calculated binding energy of -0.46 eV.

HCOO, COOH, HCOOH, and H₂CO₂. Formate (HCOO) prefers the bidentate configuration, in which the center of the molecule sits over the SB site and the two O atoms bind to two adjacent top sites (Figure 2g), with a binding energy of -3.67 eV. Its isomer, carboxyl (COOH), prefers the SB site in the *trans*-configuration via its C end (Figure 2h; BE = -2.68 eV) and is 0.62 eV less stable in energy than HCOO*. Formic acid (HCOOH) adsorbs on the top Ni site via its O end (Figure 2i), with a binding energy of -0.72 eV. Dioxymethylene (H₂CO₂) prefers to bind through both O atoms to the SB-SB site across the surface trench (Figure 2j; BE = -5.14 eV). The strong binding between the two O atoms of H₂CO₂* with the surface Ni atoms results in H₂CO₂* being 0.59 eV more stable than HCOOH*, even though H₂CO₂ is 3.83 eV less stable than HCOOH in the gas phase.

CH₂O, CH₃O, CH₂OH, CH₃O₂, and CH₃OH. Formaldehyde (CH₂O) prefers the SB-SB site across the surface trench through both the C and O atoms (Figure 2k; BE = -1.32 eV). Methoxy (CH₃O) binds via its O end to the surface; the SB site is the most favorable with a calculated BE of -2.92 eV (Figure 2l). In its preferred binding structure, the C-O bond tilts from the surface normal at an angle of 48°. The most stable adsorption site for hydroxymethyl (CH₂OH) is the top-top site (bidentate) on the surface ridge (Figure 2m; BE = -2.07 eV); the molecule is adsorbed to the surface via both the C and O atoms. For hydroxymethoxy (CH₃O₂) adsorption,

the most stable configuration is the binding over the SB-top site via its O ends across the surface trench (Figure 2n; BE = -3.00 eV). Methanol (CH_3OH) binds to the top site on the surface via its O end with a calculated BE of -0.47 eV (Figure 2o). This is similar to the binding configuration of methanol on Cu(111).

CO_3 and HCO_3 . For CO_3 adsorption, the lying-down configuration above the surface trench is the most stable with two O atoms bound at top sites on one surface ridge and the third O atom bound at the SB site on the adjacent ridge (Figure 2p). The calculated binding energy of the lying-down configuration is -5.42 eV, which is 0.23 eV more stable than the perpendicular configuration at SB-SB site across the surface trench. HCO_3 also prefers the lying-down configuration above the surface trench with a slightly different geometry than that of CO_3 : both O ends of the molecule bind to the SB sites on two adjacent ridges, and the OH group points upward, away from the surface (Figure 2q). For HCO_3^* , the lying-down configuration above the trench (BE = -3.30 eV) is more stable than the SB-SB site across the surface trench (BE = -2.95 eV).

HCOOCH_3 and H_2COOCH_3 . The most stable binding configuration of methyl formate (HCOOCH_3) is the top site with the oxygen end of methyl formate bound to an atop Ni atom (Figure 2r; BE = -0.29 eV), similar to the binding geometry of formic acid. Our results find that

H_2COOCH_3 prefers the SB-SB site (via its two oxygen atoms) across the surface trench (Figure 2s), similar to adsorbed state of H_2CO_2 . The calculated binding energy of H_2COOCH_3 is -2.93 eV.

HCO, COH, and HCOH. The most stable HCO adsorption site is the SB-SB across the surface trench via both the C and O atoms (Figure 2t), with a binding energy of -2.67 eV. Its isomer COH prefers to bind through the C atom to the PT site with a binding energy of -4.17 eV (Figure 2u). Note that in the gas phase, HCO is 1.86 eV more stable than COH; while adsorbed on the Ni(110), HCO^* is only 0.36 eV more stable than COH^* . On the basis of total electronic energy, past DFT studies have shown that COH^* is the preferred isomer over HCO^* on Ni(111), Ni(100), and stepped Ni surfaces (e.g., Ni(211), Ni(321)).^{64,65} The unique preference for the HCO^* isomer on Ni(110) could be due to the surface structure of the (110) facet, which allows for a particularly stable SB-SB adsorbate structure for HCO^* across the surface trench (Figure 2t). Such an adsorption structure is not possible on the other Ni surfaces. For HCOH^* , the most stable adsorption site is the SB site via its C end with a binding energy of -3.33 eV (Figure 2v).

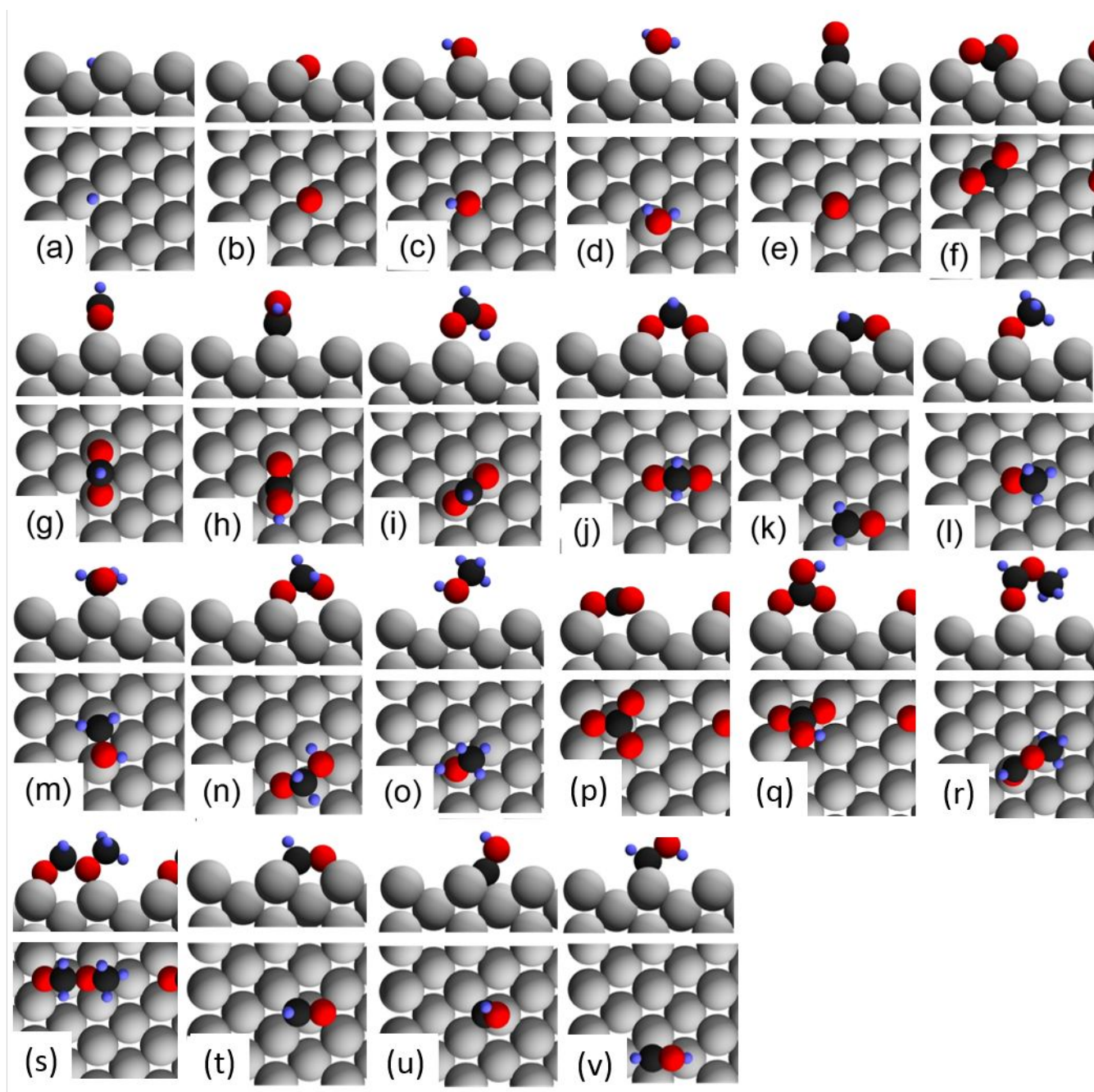


Figure 2. Cross-section and top views of the most stable adsorbed structures on Ni(110) for (a) H, (b) O, (c) OH, (d) H₂O, (e) CO, (f) CO₂, (g) HCOO, (h) COOH, (i) HCOOH, (j) H₂CO₂, (k) CH₂O, (l) CH₃O, (m) CH₂OH, (n) CH₃O₂, (o) CH₃OH, (p) CO₃, (q) HCO₃, (r) HCOOCH₃, (s) H₂COOCH₃, (t) HCO, (u) COH, and (v) HCOH. Blue, black, red, and gray spheres denote H, C, O, and Ni atoms, respectively.

Table 1. Preferred adsorption sites and respective binding energies of adsorbed species on Ni(110). Notation on binding sites: PT for pseudo three-fold, SB for short bridge, and t for top.

Species	Preferred binding site	BE(eV)	Species	Preferred binding site	BE (eV)
H*	PT	-2.74	CH ₃ O*	SB	-2.92
O*	PT	-5.30	CH ₂ OH*	t-t (ridge)	-2.07
OH*	SB (tilted)	-3.67	CH ₃ O ₂ *	SB-t (trench)	-3.00
H ₂ O*	top	-0.46	CH ₃ OH*	top	-0.47
CO*	SB	-1.92	CO ₃ *	t-t-SB	-5.42
CO ₂ *	V-shape	-0.46	HCO ₃ *	t-SB	-3.30
HCOO*	t-t (ridge)	-3.67	HCOOCH ₃ *	top	-0.29
COOH*	SB (trans)	-2.68	H ₂ COOCH ₃ *	SB-SB (trench)	-2.93
HCOOH*	top	-0.72	HCO*	SB-SBb	-2.67
H ₂ CO ₂ *	SB-SB (trench)	-5.14	COH*	PT	-4.17
CH ₂ O*	SB-SB (trench)	-1.32	HCOH*	SB	-3.33

3.2. Elementary Steps

Having calculated the structure and energetics of adsorbed intermediates, we now move on to investigate the energetics of methanol synthesis on Ni(110), including transition states structures for 51 elementary steps in total. Our results on the reaction energies and energy barriers for these elementary steps are summarized in Table 2. In the following, we discuss the most important steps in detail.

3.2.1. WGS reaction and formic acid formation

For industrial methanol synthesis, CO_2 , CO , and H_2 are the reactants. Besides methanol, formic acid can also be formed from hydrogenation of CO_2 ($\text{H}_2 + \text{CO}_2 \rightarrow \text{HCOOH}$). In addition, the WGS reaction ($\text{CO} + \text{H}_2\text{O} \rightarrow \text{CO}_2 + \text{H}_2$) may occur, which governs the conversion between CO and CO_2 . We thus first discussed the elementary steps for the WGS reaction and for formic acid formation. These relevant elementary steps are indicated by R9 to R20 in Table 2.

(1) Water activation

First H abstraction from H_2O . The first H abstraction (R9, $\text{H}_2\text{O}^* \rightarrow \text{OH}^* + \text{H}^*$) is exothermic by 0.49 eV, and an energy barrier of 0.89 eV needs to be overcome. During the reaction, one O—H bond of the adsorbed H_2O at the top site is broken; the reaction ends up with OH and H sitting at neighboring SB sites. At the transition state, the reactive O—H bond is elongated to 1.51 Å as compared with the O—H bond length of 0.98 Å in H_2O^* . Compared with that on Cu(111) (with $E_a = 1.39$ eV),^{7,35} the first H abstraction from H_2O is easier on Ni(110).

OH dissociation. The dissociation of hydroxyl (OH^*) to O^* and H^* (R10, $\text{OH}^* \rightarrow \text{O}^* + \text{H}^*$) needs to overcome a barrier of 1.01 eV, and the reaction is endothermic by 0.37 eV. During the reaction, the O—H bond is elongated and finally broken, which brings the H^* to the PT site of an adjacent row and leaves the O at the SB site. At the transition state, the O—H bond is

elongated to 1.50 Å compared to 0.98 Å in OH*, and the distance between H and each of its three neighboring Ni atoms is 1.87 Å. Similar to the first H abstraction, OH dissociation is much easier on Ni(110) than on Cu(111): the corresponding energy barrier of OH dissociation on Cu(111) is 1.68 eV.³⁵

OH+OH disproportionation. OH* + OH* disproportionation to H₂O* and O* (R11, OH* + OH* → H₂O* + O*) is controlled by its thermochemistry. The disproportionation step itself requires an energy barrier of 0.49 eV. Starting from the initial state with two OH sitting at SB sites at two adjacent ridges, one OH moves close to the other, picks up the H to form H₂O and leave an O behind. However, due to the strong attractive interaction between the H₂O* and O* species formed, the subsequent diffusion of these two species to the infinitely separated state is energetically uphill by 0.39 eV. Overall, this step is endothermic by 0.86 eV. Since the endothermicity is larger than the calculated barrier, we consider the apparent barrier of this step to be equal to its reaction energy of +0.86 eV. Compared to the calculated barrier of 0.61 eV on Cu(111),³⁵ the OH* + OH* disproportionation step is more difficult on Ni(110).

(2) CO oxidation

CO oxidation with atomic O. CO oxidation with atomic O* (R12, CO* + O* → CO₂*) is endothermic ($\Delta E = 0.40$ eV) and highly activated ($E_a = 1.57$ eV) on Ni(110). Initially, CO binds

to an SB site, and O binds to a nearby PT site. This step proceeds with the diffusion of O* to the SB site adjacent to the CO* species. O* then moves even closer to CO* to start forming a second C-O bond. At the transition state, the C—O distance is 1.77 Å. Compared with the same elementary step on Ni(111) ($E_a = 0.83$ eV)⁶³ and on Cu(111) ($E_a = 0.65$ eV)^{7,35}, CO oxidation on Ni(110) is much more difficult.

Carboxyl formation. Carboxyl (COOH*) formation from CO* and OH* (R13, $\text{CO}^* + \text{OH}^* \rightarrow \text{COOH}^* + *$) is endothermic ($\Delta E = 0.93$ eV), with an activation energy barrier of 2.00 eV. We have discussed the reverse step on Ni(110), i.e., $\text{COOH}^* + * \rightarrow \text{CO}^* + \text{OH}^*$, in detail in our previous work.⁶⁶ Compared with carboxyl formation on Cu(111), which needs a much lower barrier of 0.56 eV,³⁵ carboxyl formation on Ni(110) is very difficult.

Carboxyl decomposition. COOH* decomposition to CO₂* and H* (R14, $\text{COOH}^* \rightarrow \text{CO}_2^* + \text{H}^*$) is exothermic ($\Delta E = -0.17$ eV) and is characterized by a moderate barrier of 0.95 eV. For further information, please refer to our prior work.⁶⁶ We note that the barrier of Step R14 is smaller than the corresponding value (1.23 eV) on Cu(111), indicating that carboxyl decomposition is easier on Ni(110) than on Cu(111).

Carboxyl disproportionation by OH. Spontaneous COOH* disproportionation by OH* to CO₂* and H₂O* was reported on Cu(111).^{7,35} Here, we consider the possibility of this step (R15,

$\text{COOH}^* + \text{OH}^* \rightarrow \text{CO}_2^* + \text{H}_2\text{O}^*$) on Ni(110). The disproportionation process is nearly spontaneous with a small barrier of 0.06 eV. Subsequent diffusion of the CO_2^* and H_2O^* species to infinite separation is energetically uphill, which leads to an overall positive reaction energy of 0.32 eV. Therefore, this step is controlled by its thermochemistry. The relative small endothermicity, though, indicates that this step can be facile on Ni(110).

(3) Formate formation

Formate (HCOO) formation by CO_2^* hydrogenation (R16, $\text{CO}_2^* + \text{H}^* \rightarrow \text{HCOO}^*$) on Ni(110) is a two-step process. First, a bidentate structure at the LB site is formed, with an activation energy barrier of 0.37 eV and a reaction energy of -0.42 eV. The bidentate HCOO^* at the LB site can transform to a slightly more stable bidentate configuration (by -0.03 eV) at the SB site, with a barrier of 0.60 eV. Overall, CO_2 hydrogenation to formate is exothermic by 0.45 eV, and an effective barrier of 0.37 eV is required. By comparison, CO_2 hydrogenation to carboxyl (COOH) (i.e., the reverse reaction of R14) is endothermic ($\Delta E = 0.17$ eV) and is characterized by a higher barrier of 1.12 eV. For a more detailed discussion on formate formation, please refer to our previous work.⁶⁶ As compared to that on Cu(111) (with the calculated barrier of 0.87 eV),³⁵ formate formation on Ni(110) is easier.

We also considered formate formation through the combination of CO_2^* and H^* via a carbonate (CO_3^*) intermediate, which was experimentally observed on the step sites of Cu-deposited Pt(111).⁶⁷ Waugh proposed a mechanism in which CO_3^* can be further converted to formate through a disproportionation step with H^* ($\text{H}^* + \text{CO}_3^* \rightarrow \text{HCOO}^* + \text{O}^*$).⁶⁸ The availability of atomic O^* on the surface is key to the formation of CO_3^* . Atomic O^* can be provided by CO_2^* dissociation. Similarly as on Cu(111), we found that CO_2 does not adsorb dissociatively on Ni(110). The dissociation of CO_2^* has a high activation energy barrier of 1.17 eV, and the reaction is exothermic by 0.40 eV (see the reverse reaction of step R12). Carbonate formation via CO_2^* and atomic O^* (R17, $\text{CO}_2^* + \text{O}^* \rightarrow \text{CO}_3^* + *$) is exothermic ($\Delta E = -0.38$ eV) with a modest barrier of 0.92 eV. By comparing the formation of CO_3^* intermediate with formate formation directly from CO_2^* and H^* ($\Delta E = -0.45$ eV, $E_a=0.37$ eV), we can conclude that the direct CO_2^* hydrogenation by adsorbed H^* is the favorable path for formate formation on Ni(110).

(4) Formic acid formation

Formic acid (HCOOH) can be formed by hydrogenating either the HCOO or the COOH intermediate. Formation of formic acid by hydrogenation of HCOO (R19, $\text{HCOO}^* + \text{H}^* \rightarrow \text{HCOOH}^*$) is endothermic by 0.93 eV and needs to overcome a barrier of 1.32 eV. HCOOH^* formation via COOH^* hydrogenation (R20, $\text{COOH}^* + \text{H}^* \rightarrow \text{HCOOH}^*$) has a reaction energy of

0.34 eV and an energy barrier of 0.89 eV. More detailed discussion of these two elementary steps can be found in our previous work.⁶⁶

(5) Potential energy diagram and reaction network

We plotted the potential energy diagram (PED) for the WGS reaction and formic acid formation on Ni(110) in Figure 3. The reaction network for the WGS reaction and formic acid formation is also illustrated in Figure 4. As we can see clearly from Figures 3 and 4, for the WGS reaction on Ni(110), the redox mechanism (black line) is energetically favored over the carboxyl-mediated mechanism (red line), mainly because the formation of carboxyl from CO* and OH* is extremely difficult on Ni(110) (R13, $E_a = 2.00$ eV). This is in sharp contrast to the WGS reaction on Cu^{7,35} and Pd⁶⁹ catalysts, where the carboxyl-mediated mechanism dominates. Although the OH* disproportionation step on Ni(110) requires a lower barrier (R11, 0.86 eV) than the direct OH* dissociation (R10, 1.01 eV), this step is thermodynamically uphill, which increases the apparent barrier of the subsequent CO₂* formation step. Overall, the disproportionation pathway (purple line in Figure 3) is also unfavorable compared to the redox pathway. The formic acid formation from CO₂ hydrogenation has been discussed in detail in our previous work.⁶⁶ The first hydrogenation step prefers a formate path, as formate (Intermediate (22)) is 0.62 eV more stable

than its isomer carboxyl (Intermediate (11)), and a smaller energy barrier (R16, 0.37 eV) needs to be overcome.

Table 2. Elementary steps of methanol synthesis from CO and CO₂ hydrogenation on Ni(110).

[a]

No.	Reaction	E _{int} (eV)		ΔE (eV)	E _a (eV)
		IS	FS		
R1	CO ₂ + * → CO ₂ *	-	-	-0.46	
R2	H ₂ + 2* → 2H*	-	-	-0.94	
R3	CO + * → CO*	-	-	-1.92	
R4	H ₂ O + * → H ₂ O*	-	-	-0.46	
R5	HCOOH + * → HCOOH*	-	-	-0.72	
R6	CH ₂ O + * → CH ₂ O*	-	-	-1.32	
R7	CH ₃ OH + * → CH ₃ OH*	-	-	-0.47	
R8	HCOOCH ₃ + * → HCOOCH ₃ *	-	-	-0.29	
R9	H ₂ O* + * → OH* + H*	-	0.14	-0.49	0.89
R10	OH* + * → O* + H*	-	0.12	0.37	1.01
R11	2OH* → H ₂ O* + O*	-0.27	-0.39	0.86	0.86 ^[b]
R12	CO* + O* → CO ₂ * + *	0.06	-	0.40	1.57
R13	CO* + OH* → COOH* + *	0.15	-	0.93	1.90
R14	COOH* + * → CO ₂ * + H*	-	-0.04	-0.17	0.95
R15	COOH* + OH* → CO ₂ * + H ₂ O*	-0.03	-0.37	0.32	0.32 ^[b]
R16	CO ₂ * + H* → HCOO* + *	-0.04	-	-0.45	0.37
R17	CO ₂ * + O* → CO ₃ * + *	0.18	-	-0.38	0.92
R18	CO ₃ * + H* → HCO ₃ * + *	0.10	-	0.04	1.15
R19	HCOO* + H* → HCOOH* + *	0.00	-	0.93	1.32
R20	COOH* + H* → HCOOH* + *	0.08	-	0.34	0.89
R21	HCOOH* + H* → CH ₃ O ₂ * + *	0.00	-	0.02	0.66
R22	CH ₃ O ₂ * + * → CH ₂ O* + OH*	-	0.24	-0.35	0.84
R23	CH ₃ O ₂ * + * → CH ₂ OH* + O*	-	-0.07	0.46	1.88
R24	CH ₂ O* + OH* → CH ₃ O* + O*	0.24	-0.07	0.33	0.92
R25	CH ₂ O* + H* → CH ₃ O* + *	0.09	-	-0.04	0.69
R26	CH ₃ O* + H* → CH ₃ OH* + *	0.05	-	0.56	1.53
R27	CH ₂ O* + H* → CH ₂ OH* + *	0.09	-	0.44	1.07
R28	CH ₂ OH* + H* → CH ₃ OH* + *	0.13	-	0.06	0.82
R29	CH ₃ O* + OH* → CH ₃ OH* + O*	-0.30	-0.46	0.90	0.90 ^[b]
R30	CH ₃ O* + HCOO* → HCOOCH ₃ * + O*	0.04	-0.13	1.59	1.94
R31	2CH ₂ O* → HCOOCH ₃ * + *	0.28	-	0.58	1.83
R32	HCOO* + H* → H ₂ CO ₂ * + *	0.00	-	0.30	1.20
R33	H ₂ CO ₂ * + * → CH ₂ O* + O*	-	-0.02	0.64	1.45
R34	H ₂ CO ₂ * + H* → CH ₃ O ₂ * + *	0.08	-	0.63	1.34
R35	HCOOCH ₃ * + H* → H ₂ COOCH ₃ * + *	0.30	-	-0.01	1.13
R36	CH ₃ O* + CH ₂ O* → H ₂ COOCH ₃ * + *	0.24	-	0.42	0.90
R37	CO* + H* → HCO* + *	-0.01	-	0.85	1.06
R38	CO* + H* → COH* + *	-0.01	-	1.20	1.45
R39	HCOO* + * → HCO* + O*	-	0.18	0.86	1.55
R40	HCOOH* + * → HCO* + OH*	-	0.03	-0.42	0.45
R41	HCO* + H* → CH ₂ O* + *	-0.02	-	0.10	0.52

R42	$\text{HCO}^* + \text{H}^* \rightarrow \text{HCOH}^* + *$	-0.02	-	0.38	0.90
R43	$\text{HCOOH}^* + * \rightarrow \text{HCOH}^* + \text{O}^*$	-	0.01	0.32	1.47
R44	$\text{HCOH}^* + \text{H}^* \rightarrow \text{CH}_2\text{OH}^* + *$	-0.04	-	0.16	0.48
R45	$\text{O}^* + \text{HCO}^* \rightarrow \text{OH}^* + \text{CO}^*$	0.09	0.15	-1.20	- [c]
R46	$\text{OH}^* + \text{HCO}^* \rightarrow \text{H}_2\text{O}^* + \text{CO}^*$	0.03	-0.20	-0.76	0.93
R47	$\text{HCOO}^* + \text{HCO}^* \rightarrow \text{HCOOH}^* + \text{CO}^*$	0.04	-0.08	0.08	- [d]
R48	$\text{HCOO}^* + \text{HCO}^* \rightarrow \text{H}_2\text{CO}_2^* + \text{CO}^*$	0.04	0.14	-0.51	- [e]
R49	$\text{HCOOH}^* + \text{HCO}^* \rightarrow \text{CH}_3\text{O}_2^* + \text{CO}^*$	-0.04	0.06	-0.90	1.04 [f]
R50	$\text{CH}_2\text{O}^* + \text{HCO}^* \rightarrow \text{CH}_3\text{O}^* + \text{CO}^*$	0.16	-0.03	-0.88	- [g]
R51	$\text{CH}_3\text{O}^* + \text{HCO}^* \rightarrow \text{CH}_3\text{OH}^* + \text{CO}^*$	-0.07	-0.17	-0.45	0.90

[a] ΔE and E_a are the calculated reaction energies and energy barriers, evaluated with respect to species in the initial/final state at infinite separation. E_{int} describes the interaction between co-adsorbed species; a positive E_{int} value indicates repulsive interaction, and *vice versa*. Steps R1 – R8 are adsorption steps associated with zero energy barriers.

[b] The forward reactions of Steps R11, R15, and R29 are controlled by their thermochemistry, and the barriers are equal to the reaction energies.

[c] Step R45 includes two sequential steps: the facile HCO^* decomposition, $\text{HCO}^* \rightarrow \text{H}^* + \text{CO}^*$ (inverse R37) and $\text{H}^* + \text{O}^* \rightarrow \text{OH}^*$ (inverse R10).

[d] Step R47 involves two sequential steps: HCO^* decomposition, $\text{HCO}^* \rightarrow \text{H}^* + \text{CO}^*$ (inverse R37) followed by step R19, $\text{H}^* + \text{HCOO}^* \rightarrow \text{HCOOH}^*$.

[e] Step R48 is sequential and includes two sub-steps: HCO^* decomposition, $\text{HCO}^* \rightarrow \text{H}^* + \text{CO}^*$ (inverse R37) and $\text{H}^* + \text{HCOO}^* \rightarrow \text{H}_2\text{CO}_2^*$ (step R32).

[f] This concerted step is not favorable over the sequential steps including inverse step R37, $\text{HCO}^* \rightarrow \text{H}^* + \text{CO}^*$, and step R21, $\text{H}^* + \text{HCOOH}^* \rightarrow \text{CH}_3\text{O}_2^*$.

[g] This is not a concerted step. It is sequential and includes HCO^* decomposition, $\text{HCO}^* \rightarrow \text{H}^* + \text{CO}^*$ (inverse R37) and step R25, $\text{CH}_2\text{O}^* + \text{H} \rightarrow \text{CH}_3\text{O}^*$.

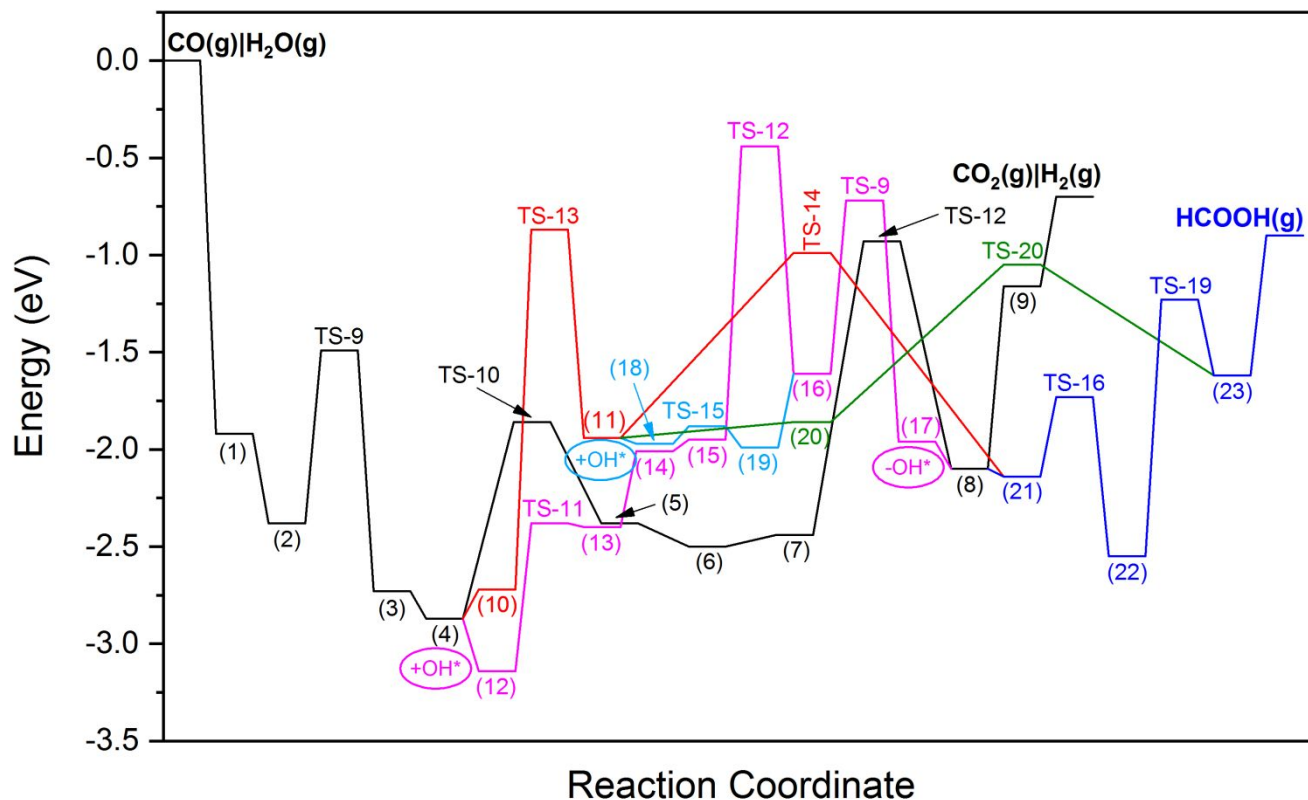
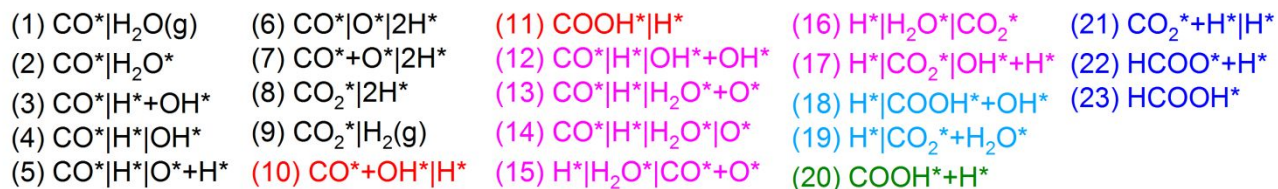


Figure 3. Potential energy diagram of the WGS reaction and formic acid formation on Ni(110). The black, red, and purple lines denote the redox pathway, the carboxyl pathway, and the disproportionation pathway for WGS, respectively. The cyan line denotes the decomposition of COOH^* through disproportionation with OH^* . The blue and green lines denote the formic acid formation via the hydrogenation of HCOO^* and COOH^* , respectively. Intermediates are labelled as (1) – (23). Gas-phase and adsorbed species are denoted with (g) and *, respectively. Symbols + and | indicate co-adsorbed species and species at infinite separation, respectively. TS- n denotes the transition state of reaction step R/n in Table 2. The total energy of gas-phase CO and H_2O is set to zero.

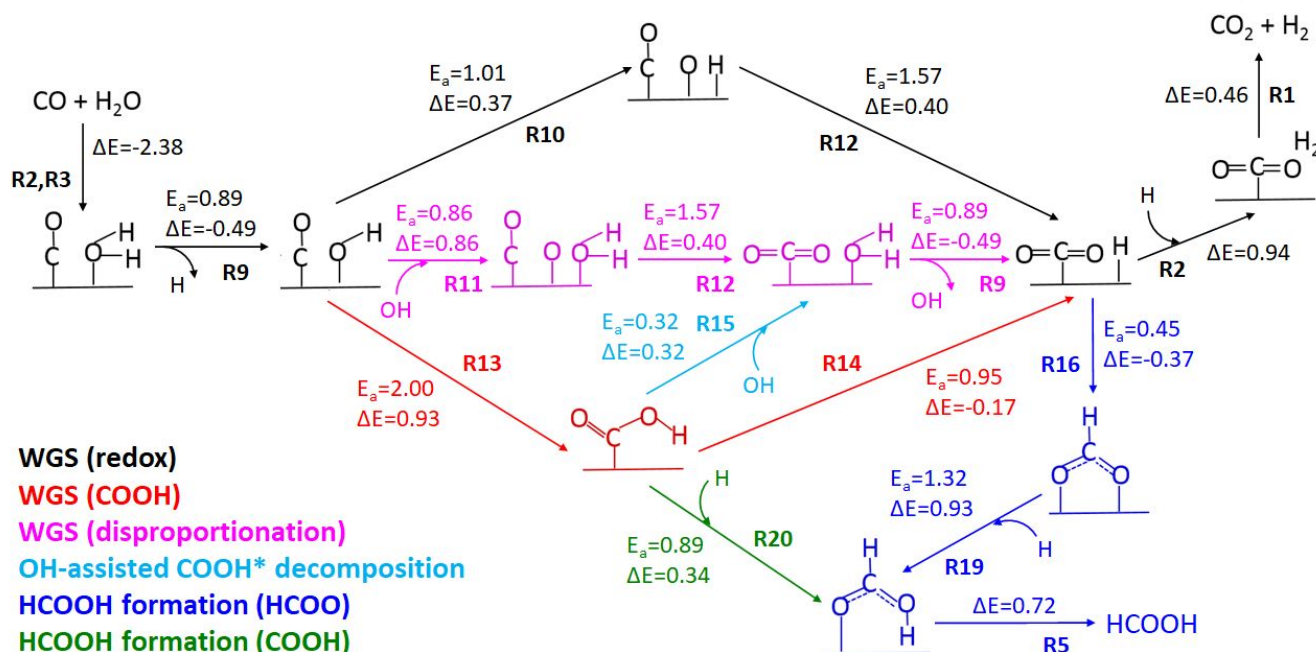


Figure 4. Reaction network for the WGS reaction and formic acid formation on Ni(110). The reaction energies (ΔE) and the activation energy barriers (E_a) for all the elementary steps are given in eV. Label R_n refers to the elementary step given in Table 2.

3.2.2. Methanol synthesis via formic acid path

We now turn our attention to the elementary steps for methanol synthesis via the formic-acid-mediated path. The relevant elementary steps are listed as R21 to R31 in Table 2.

(1) **Hydroxymethoxy (CH_3O_2) formation via formic acid (HCOOH) hydrogenation.** Along the formic-acid-mediated pathway for methanol synthesis, HCOOH is first hydrogenated to hydroxymethoxy (CH_3O_2). Shown in Figure 5(a) is the potential energy diagram of hydroxymethoxy formation via formic acid hydrogenation (R21 , $\text{HCOOH}^* + \text{H}^* \rightarrow \text{CH}_3\text{O}_2^* + *$).

During the reaction, HCOOH^* is tilted towards the adsorbed H at the PT site in the adjacent row,

and the O bound on the surface moves from the top site to the SB site. At the transition state, the binding O has moved to the SB site, and the whole HCOOH* tilts away from the surface normal [see the inset in Figure 5(a)]; the adsorbed H moved upwards by 0.66 Å, resulting in a C—H distance of 1.57 Å. Further movement of HCOOH* and H* leads to the formation of a C—H bond and the binding of OH* to a top Ni atom in an adjacent row across the surface trench. As seen in Figure 5(a), the hydroxymethoxy formation via formic acid hydrogenation is nearly thermoneutral ($\Delta E = 0.02$ eV) and has a barrier of 0.66 eV. Remarkably, compared with that on Cu(111) ($E_a = 1.04$ eV),³⁵ the barrier of HCOOH hydrogenation to CH₃O₂ on Ni(110) is much lower.

Hydroxymethoxy (CH₃O₂) is one of the key intermediate species for methanol synthesis on Cu(111).³⁵ Later, we show that this is also likely the case on Ni(110). We calculated the vibrational frequencies and simulated the infrared spectrum of CH₃O₂* on Ni(110). The calculated vibrational frequencies are tabulated in Table S1, and the simulated infrared spectrum is shown in Figure 5(b). We found a sharp peak associated with the stretching mode of CO₂ in that intermediate at 1049 cm⁻¹. Interestingly, the bending mode of CH₂ at 1002 cm⁻¹ appears as a shoulder of the CO₂ stretching mode. The intensity of the C—OH rotation mode at 553 cm⁻¹ is close to that of the stretching modes of CH₂ and OH at 2946 cm⁻¹ and 3441 cm⁻¹,

respectively. The soft CO_2 rocking mode at 448 cm^{-1} and the O—surface stretching mode at 317 cm^{-1} also appear as small peaks in the simulated infrared spectrum.

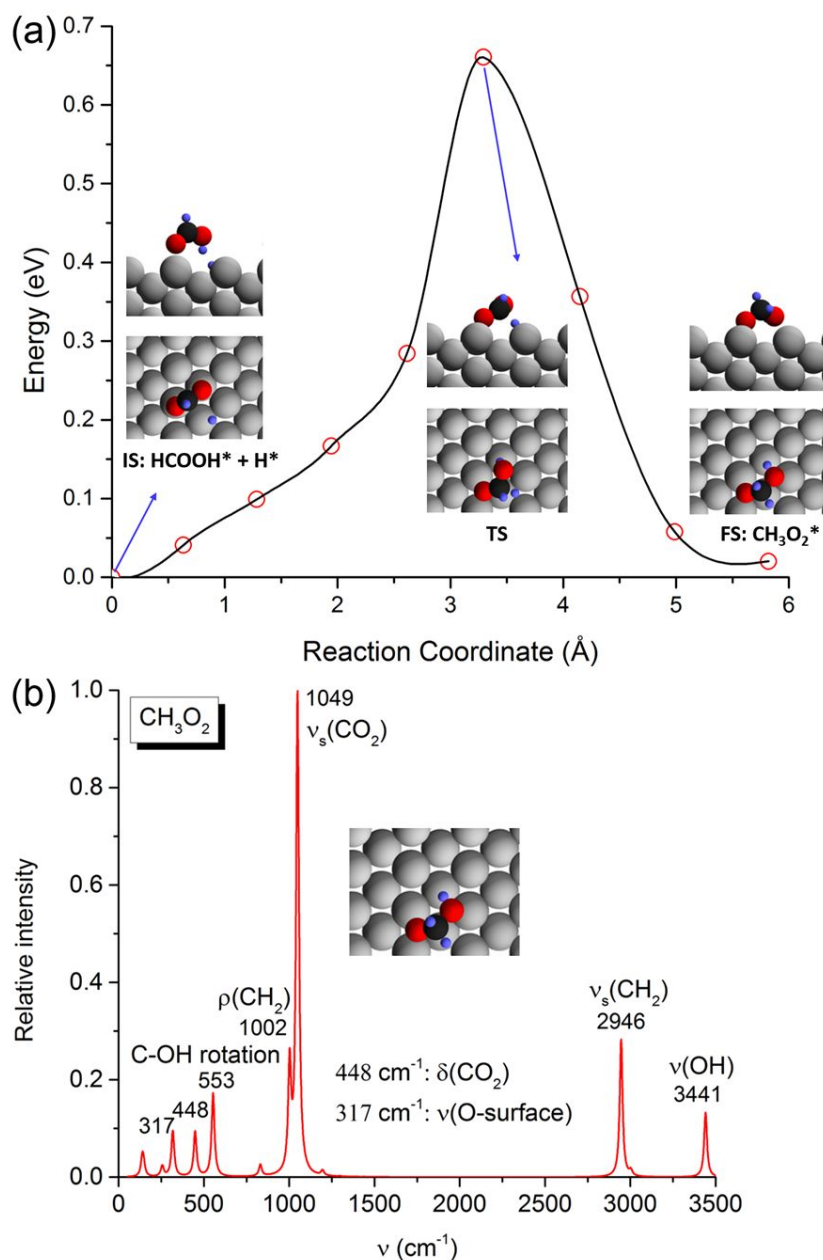


Figure 5. (a) Potential energy diagram of hydroxymethoxy (CH_3O_2) formation via formic acid (HCOOH) hydrogenation on Ni(110). Top and cross-section views of the atomic structure of the initial state (IS), transition-state (TS), and final state (FS) are shown in insets. Blue, black, red, and gray spheres denote H, C, O, and Ni atoms, respectively. (b) Simulated infrared spectrum

of hydroxymethoxy (CH_3O_2) on Ni(110). A Lorentzian broadening of 20 cm^{-1} has been used. ν : stretch (ν_s , symmetric); δ : bend; ρ : rock.

(2) Hydroxymethoxy (CH_3O_2) decomposition

Hydroxymethoxy (CH_3O_2) decomposition to formaldehyde (CH_2O) and hydroxyl (OH). Once CH_3O_2^* is formed, the next step towards formation of the product methanol is the C—OH bond breaking in CH_3O_2^* to form formaldehyde CH_2O^* and OH^* (R22, $\text{CH}_3\text{O}_2^* + * \rightarrow \text{CH}_2\text{O}^* + \text{OH}^*$). This step is exothermic ($\Delta E = -0.35 \text{ eV}$) with a barrier of 0.84 eV . At the transition state, the C—OH bond is significantly stretched (the length of C—OH is 2.53 \AA). Further movement leads to the formation of a C—Ni bond and brings OH^* to the SB site.

Hydroxymethoxy (CH_3O_2) decomposition to CH_2OH and O . We also considered a different step for CH_3O_2^* decomposition, i.e., $\text{CH}_3\text{O}_2^* \rightarrow \text{CH}_2\text{OH}^* + \text{O}^*$ (R23). This step is endothermic by 0.46 eV and has a higher energy barrier of 1.88 eV . Thus, it is clearly less favorable than Step $\text{CH}_3\text{O}_2^* \rightarrow \text{CH}_2\text{O}^* + \text{OH}^*$ (R22).

(3) Methoxy (CH_3O) formation via formaldehyde (CH_2O) hydrogenation. The next step toward the final product methanol is hydrogenation of CH_2O^* to CH_3O^* (R25, $\text{CH}_2\text{O}^* + \text{H}^* \rightarrow \text{CH}_3\text{O}^* + *$). This elementary step is slightly exothermic by 0.04 eV , and with a moderate barrier of 0.69 eV . Alternatively, CH_2O^* can be hydrogenated to CH_3O^* using OH^* as the source of H, leaving an atomic O^* on the surface (R24, $\text{CH}_2\text{O}^* + \text{OH}^* \rightarrow \text{CH}_3\text{O}^* + \text{O}^*$). This alternative step is

endothermic by 0.33 eV and has a barrier of 0.92 eV, 0.23 eV higher than that of the direct hydrogenation step (R25). Therefore, direct hydrogenation is the preferred path for CH_2O^* hydrogenation to CH_3O^* .

(4) Methanol (CH_3OH) formation via methoxy (CH_3O) hydrogenation. Hydrogenation of methoxy CH_3O^* is the final step to methanol production (R26, $\text{CH}_3\text{O}^* + \text{H}^* \rightarrow \text{CH}_3\text{OH}^* + *$). This step was found to be the rate-determining step for methanol synthesis on $\text{Cu}(111)$.^{35,70} Plotted in Figure 6 is the calculated potential energy diagram for methanol formation via methoxy hydrogenation. During the reaction, the CH_3 moiety tilts towards the adsorbed H, followed by the movement of O from the SB site to the top site; the adsorbed H^* moves up closer to O as well. At the transition state, the H—O distance is 1.47 Å. Further movement of CH_3O^* and H^* ends up with the formation of an O—H bond, and the product CH_3OH^* binds to the top site. This step is endothermic ($\Delta E = 0.56$ eV) with a barrier of 1.53 eV. As compared with the calculated barrier of 1.17 eV for the same step on $\text{Cu}(111)$,³⁵ methanol formation via methoxy hydrogenation is more difficult on $\text{Ni}(110)$. This can be explained by the stronger binding of CH_3O^* on $\text{Ni}(110)$ than on $\text{Cu}(111)$: the calculated binding energy of CH_3O^* is -2.92 eV on $\text{Ni}(110)$ while the corresponding value is -2.45 eV on $\text{Cu}(111)$.³⁵ As a result, more energy is required on $\text{Ni}(110)$ to weaken the binding of CH_3O^* in order to bring it to the bond-making transition state.

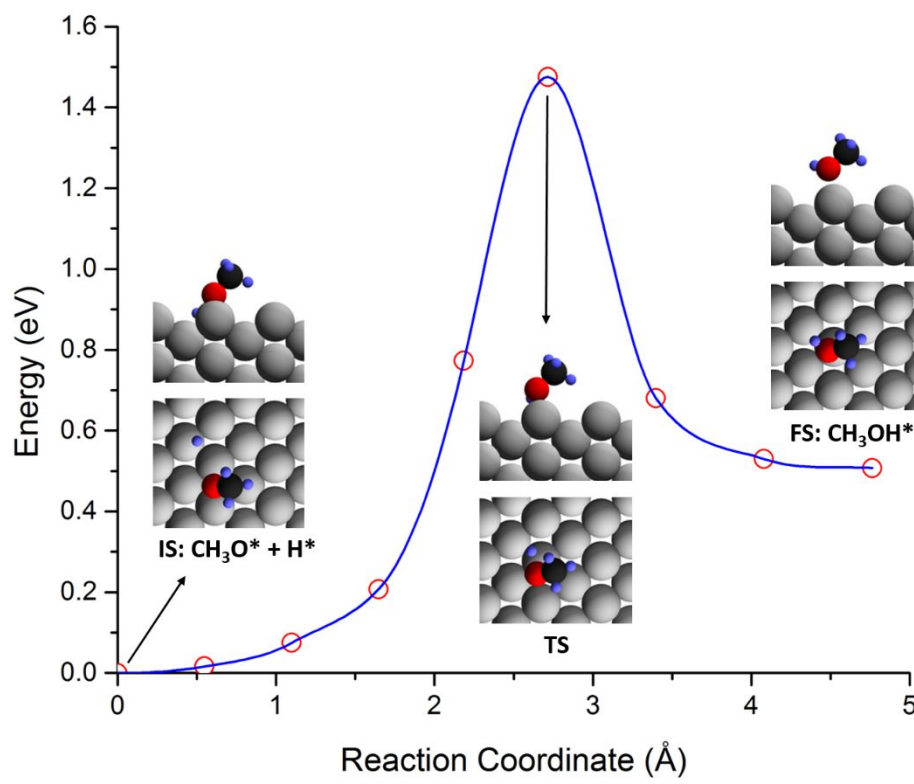


Figure 6. Potential energy diagram for methanol (CH_3OH) formation via methoxy (CH_3O) hydrogenation on Ni(110). Top and cross-section views of the atomic structure of the initial state (IS), transition-state (TS) and final state (FS) are shown in the insets. Blue, black, red, and gray spheres denote H, C, O, and Ni atoms, respectively.

(5) Methanol (CH_3OH) formation via CH_2OH hydrogenation. Note that instead of the sequence of steps: $\text{CH}_2\text{O}^* + \text{H}^* \rightarrow \text{CH}_3\text{O}^* + *$ (R25) and $\text{CH}_3\text{O}^* + \text{H}^* \rightarrow \text{CH}_3\text{OH}^*$ (R26), an alternative route to methanol from CH_2O^* exists, that is, $\text{CH}_2\text{O}^* + \text{H}^* \rightarrow \text{CH}_2\text{OH}^* + *$ (R27) followed by $\text{CH}_2\text{OH}^* + \text{H} \rightarrow \text{CH}_3\text{OH}^*$ (R28). On Ni(110), hydroxymethyl (CH_2OH^*) is 0.33 eV less stable than methoxy CH_3O^* . Compared with the exothermic reaction of R25 ($\Delta E = -0.04$ eV, $E_a = 0.69$ eV), Step R27 is endothermic by 0.44 eV with a higher barrier of 1.07 eV. The CH_2OH^* formation is thus both thermodynamically and kinetically less favorable than the CH_3O^* formation. However,

we notice that further hydrogenation of CH_2OH^* to CH_3OH^* (R28) is slightly endothermic ($\Delta E = 0.06$ eV) with a barrier of $E_a = 0.82$ eV, which is easier than $\text{CH}_3\text{O}^* + \text{H}^* \rightarrow \text{CH}_3\text{OH}^*$ (R26, $E_a = 1.53$ eV).

(6) Methanol (CH_3OH) formation from methoxy (CH_3O) and hydroxyl (OH). We also considered hydrogenation of CH_3O^* using OH^* as the H^* source, $\text{CH}_3\text{O}^* + \text{OH}^* \rightarrow \text{CH}_3\text{OH}^* + \text{O}^*$ (R29). This step is controlled by its thermochemistry with an endothermicity of 0.90 eV. The bond-making/breaking process itself requires an energy barrier of 0.48 eV, which is smaller than the overall reaction energy. The endothermicity of this step is mainly caused by the large attractive interaction ($E_{\text{int}} = -0.46$ eV) between the two species, CH_3OH^* and O^* , in the final state. The adsorbed O^* can be hydrogenated to OH^* with $\Delta E = -0.37$ eV and $E_a = 0.64$ eV (reverse reaction of step R10). The path via $\text{CH}_3\text{O}^* + \text{OH}^* \rightarrow \text{CH}_3\text{OH}^* + \text{O}^*$ (R29, $E_a = 0.90$ eV) should compete with the path via $\text{CH}_3\text{O}^* + \text{H}^* \rightarrow \text{CH}_3\text{OH}^*$ (R26, $E_a = 1.53$ eV). To close the catalytic reaction cycle, water formation from OH^* is also needed. This step is the reverse of step R9 with $\Delta E = 0.49$ eV and $E_a = 1.38$ eV.

(7) Methyl formate (HCOOCH_3) formation. Methyl formate (HCOOCH_3) is a major byproduct of methanol synthesis over Cu/SiO_2 and was observed by in-situ Fourier transform infrared spectroscopy (FTIR).⁷¹ On $\text{Cu}(110)$ predosed with O^* , dissociation of HCOOCH_3 to CH_3O^* and

HCOO^* ($\text{HCOOCH}_3^* + \text{O}^* \rightarrow \text{CH}_3\text{O}^* + \text{HCOO}^*$) was suggested.⁷² On Ni(110), HCOOCH_3^* formation ($\text{CH}_3\text{O}^* + \text{HCOO}^* \rightarrow \text{HCOOCH}_3^* + \text{O}^*$, R30) is endothermic by 1.59 eV and has a barrier of 1.94 eV. As a comparison, on Cu(111), this step is endothermic by 0.99 eV with an energy barrier of 1.24 eV.³⁵ On Ni(110), formation of HCOOCH_3^* via two CH_2O^* ($2\text{CH}_2\text{O}^* \rightarrow \text{HCOOCH}_3^*$, R31) is endothermic ($\Delta E = 0.58$ eV) with a high barrier of 1.83 eV. Since both R30 and R31 steps are highly activated, it is unlikely for HCOOCH_3 to form on Ni(110).

3.2.3. Methanol synthesis via dioxymethylene path

In this section, we discuss the elementary steps of methanol synthesis via an alternative path mediated by dioxymethylene (H_2CO_2) instead of formic acid. The relevant elementary steps are listed as R32 to R34 in Table 2.

(1) Dioxymethylene (H_2CO_2) formation. Instead of formic acid, formate can be hydrogenated at its C atom to dioxymethylene (H_2CO_2), which is a stable reaction intermediate for methanol synthesis on Cu and can be further hydrogenated to CH_3O_2^* . We found that on Ni(110), H_2CO_2^* is 0.59 eV more stable than HCOOH^* . Note that on Cu(111), HCOOH^* is more stable than H_2CO_2^* instead.³⁵ The relative stability of H_2CO_2^* over HCOOH^* is due to much stronger binding of H_2CO_2 on Ni(110): the binding strength of H_2CO_2 increases by 1.82 eV from Cu(111) to Ni(110), while the binding strength of HCOOH is enhanced by only 0.50 eV. Plotted in Figure

7(a) is the PED of formate (HCOO^*) hydrogenation to dioxymethylene (H_2CO_2^*) (R32, $\text{HCOO}^* + \text{H}^* \rightarrow \text{H}_2\text{CO}_2^* + *$) on Ni(110). This elementary step is exothermic by 0.30 eV, and the reaction barrier is 1.20 eV. Along the reaction coordinate, the bidentate formate moves from the top sites towards the SB site, while the adsorbed H moves closer to formate simultaneously. At the transition state, one O of the formate has moved to the SB site; and the distance between the adsorbed H and C is 1.54 Å. After that, the other O atom transfers to the SB site, and the adsorbed H forms a bond with C.

As dioxymethylene is a key intermediate species, we calculated its vibrational frequencies (Table S1) and simulated its vibrational spectrum (Figure 7(b)). The frequencies are close to the values of dioxymethylene on Cu.^{35,73,74} As seen in Figure 7(b), the symmetric stretching mode in CO_2 at 999 cm^{-1} has the highest intensity; the stretching mode in CH_2 at 2937 cm^{-1} and the bending mode in CO_2 at 533 cm^{-1} are also very strong. The stretching mode of O—surface at 430 cm^{-1} shows a weak peak. This vibrational spectrum provides a fingerprint for dioxymethylene and could be useful to identify dioxymethylene in future infrared experiments.

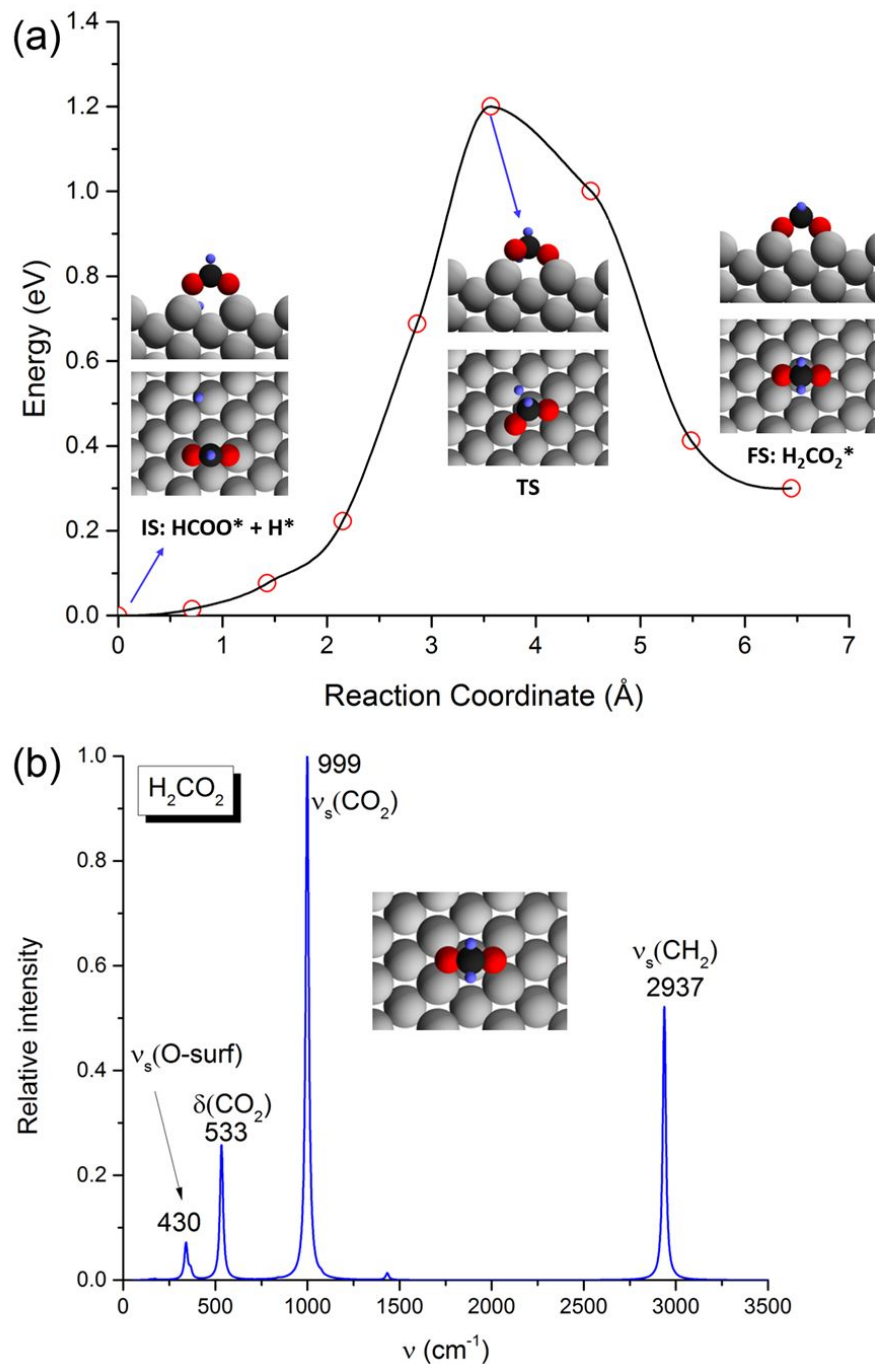


Figure 7. (a) Potential energy diagram of dioxymethylene (CH_2O_2) formation via formate (HCOO) hydrogenation on $\text{Ni}(110)$. Top and cross-section views of the atomic structure of the initial state (IS), transition-state (TS), and final state (FS) are shown in the insets. Blue, black, red, and gray spheres denote H, C, O, and Ni atoms, respectively. (b) Simulated Infrared spectrum of dioxymethylene (CH_2O_2) on $\text{Ni}(110)$. A Lorentzian broadening of 20 cm^{-1} has been used. ν_s : stretch (symmetric); δ : bend.

(2) Dioxymethylene (H_2CO_2) decomposition. The decomposition of H_2CO_2^* breaks one C—O bond to form CH_2O^* and O^* (R33, $\text{H}_2\text{CO}_2^* + * \rightarrow \text{CH}_2\text{O}^* + \text{O}^*$). This step is endothermic by 0.64 eV, with a large activation energy barrier of 1.45 eV. The O^* species formed can be hydrogenated to OH^* through the reverse reaction of step R10 as discussed earlier ($\Delta E = 0.37$ eV, $E_a = 0.64$ eV).

Once CH_2O^* is formed, it can be hydrogenated to the final product, methanol, via either CH_3O^* (R25 followed by one of the following two steps: R26 or R29) or CH_2OH^* (R27 and R28). These elementary steps are the same as those in the formic-acid-mediated path and have been discussed above.

We note in passing that H_2CO_2^* can be hydrogenated to CH_3O_2^* (R34, $\text{H}_2\text{CO}_2^* + \text{H}^* \rightarrow \text{CH}_3\text{O}_2^* + *$). This step is endothermic ($\Delta E = 0.63$ eV) with a barrier of 1.34 eV. The difference in reaction energy and energy barrier in R21 (i.e., CH_3O_2 formation via formic acid hydrogenation) and R34 is mainly because H_2CO_2^* is 0.59 eV more stable than HCOOH^* on Ni(110).

3.3. PED of Methanol Synthesis from CO_2 Hydrogenation

To summarize the elementary steps on Ni(110) discussed above, we plotted the potential energy diagram of methanol synthesis from CO_2 hydrogenation in Figure 8. The overall reaction

can be divided into two parts: (1) formation of CH_2O^* (Intermediate (8)) and (2) hydrogenation of CH_2O^* to methanol. The first part proceeds through either the formic-acid-mediated path (black line) or the dioxymethylene-mediated path (red line). Comparing the two reaction paths, we notice that H_2CO_2^* (Intermediate (16)) is 0.59 eV more stable than HCOOH^* (Intermediate (5)). The energy barrier for formate hydrogenation to H_2CO_2^* is 1.20 eV (R32), which is slightly lower than that for formate hydrogenation to formic acid (R19, $E_a = 1.32$ eV). Notice that HCOOH^* decomposition to formate (reverse of R19) is facile with a small energy barrier of 0.39 eV, while H_2CO_2^* decomposition to formate is relatively difficult (reverse of R32, $E_a = 0.90$ eV). This indicates that H_2CO_2^* may have a higher surface coverage than HCOOH^* . Further hydrogenation of H_2CO_2^* to CH_3O_2^* (R34) requires a barrier of 1.34 eV, as compared with a barrier of 0.66 eV from formic acid HCOOH^* to CH_3O_2^* (R21). Note that on Figure 8, the transition state for H_2CO_2^* hydrogenation (TS-34) and that for HCOOH^* hydrogenation (TS-21) are comparable in energy. Starting from CH_3O_2^* (Intermediate (6)), the remaining steps in the dioxymethylene-mediated path are the same as those in the formic acid-mediated path. We further notice that H_2CO_2^* hydrogenation to CH_3O_2^* is favored over H_2CO_2^* decomposition to $\text{CH}_2\text{O}^* + \text{O}^*$ (R33, cyan line). The latter has a barrier of 1.45 eV and a reaction energy of 0.62 eV. The higher surface coverage of H_2CO_2^* and the comparable transition state energy may

suggest that the reaction probability via the H_2CO_2^* -mediated path is higher than that over the HCOOH^* -mediated path. This is in sharp contrast to methanol synthesis on $\text{Cu}(111)$, where the HCOOH^* -mediated path is favored over the H_2CO_2^* -mediated path.³⁵

Once CH_2O^* is formed, there are two different routes towards the formation of the final product, methanol: the CH_3O route (blue and green lines) and the CH_2OH route (purple line). For the CH_3O route, the barriers are 0.60 eV and 1.48 eV for C—H (R25) and O—H (R26) bond formation, respectively; while for the CH_2OH route, the barriers are 0.83 eV and 0.69 eV for O—H (R27) and C—H (R28) bond formation, respectively. Note that CH_3O^* (Intermediate (10)) is 0.49 eV more stable than its isomer CH_2OH^* (Intermediate (21) on $\text{Ni}(110)$), suggesting that the probability to reach CH_3O^* is higher than that of CH_2OH^* . However, the subsequent O—H bond formation from CH_3O^* to CH_3OH^* (R26) needs a barrier as high as 1.48 eV, compared with a smaller barrier of 0.69 eV for C—H bond formation in CH_2OH to form CH_3OH^* (R28). The transition state of O—H bond formation in $\text{CH}_3\text{O}^* \rightarrow \text{CH}_3\text{OH}^*$ (TS-26) is 0.23 eV higher in energy than the transition state of C—H bond formation in $\text{CH}_2\text{OH}^* \rightarrow \text{CH}_3\text{OH}^*$ (TS-28). For the CH_3O route, we also considered the OH-assisted hydrogenation path (green line). The highest transition state along this path (TS-10) is of approximately the same energy as that of the direct hydrogenation (TS-26), indicating that these two paths coexist with similar energetics. The

combined thermodynamic and kinetic effect of CH₃O and CH₂OH routes suggests that they may compete with each other on Ni(110). This is different from the situation on Cu(111), where CH₃O is the dominant route.³⁵ The by-product, H₂O*, is formed through the combination of OH* and H* (TS-9), with an activation barrier of 1.38 eV (reverse of R9).

To complete the catalytic cycle, both products, CH₃OH* and H₂O*, need to be desorbed from the surface, with desorption energies of 0.47 eV and 0.46 eV, respectively (i.e., the absolute values of their binding energies shown in Table 1). For both product species, the desorption energy is much lower than the energy barriers for reactivating these species, which indicates that both species will readily be desorbed once formed on Ni(110). The desorption energy of CH₃OH* is 0.47 eV, significantly lower than the activation energy barriers for CH₃OH* dissociation to form both CH₃O* (reverse of R26: CH₃OH* + * → CH₃O* + H*, E_a = 0.97 eV) and CH₂O* (reverse of R28: CH₃OH* + * → CH₂OH* + H*, E_a = 0.76 eV). For H₂O*, its desorption energy is 0.46 eV, which is 0.43 eV lower than the activation energy barrier for the H₂O* dissociation step (R9: H₂O* + * → OH* + H*, E_a = 0.89 eV).

To further elucidate the reason behind the different reaction pathways observed on Ni(110) and Cu(111), we compared all the DFT-derived energetics on Ni(110) with those values obtained earlier on Cu(111) (Figures S1 and S2 in Supporting Information).³⁵ For all the adsorbed species, we observed much stronger binding on Ni(110) as compared to Cu(111) (Figure S1). This is expected due to the more reactive

nature of Ni than Cu as well as (110) being a more open facet than (111). On average, and among the 22 adsorbed species studied, the adsorption on Ni(110) is more stable by 0.95 eV. The largest difference in binding energy (1.82 eV) was observed for dioxymethylene (H_2CO_2^*), which was predicted to be involved in methanol synthesis on Ni(110). Stronger binding of surface intermediates generally leads to easier bond-breaking steps, while it makes bond-making and disproportionation steps more difficult due to the additional energy cost to bring both reactants to the transition state. With few exceptions, this prediction is in line with our calculated activation energy barriers on Ni(110) and Cu(111) (Figure S2). The barriers for bond-breaking steps are generally lower on Ni(110) than Cu(111) (Figure S2a), while those for disproportionation and bond-making steps are higher on Ni(110) than Cu(111) (Figures S2b and S2c, respectively). For example, the carboxyl formation step from CO^* and OH^* (R13: $\text{CO}^* + \text{OH}^* \rightarrow \text{COOH}^* + *$), a bond-making step, is more activated by 1.44 eV on Ni(110) than Cu(111), which explains why the WGS reaction cannot occur on Ni(110) through the carboxyl pathway, the preferred WGS pathway on Cu(111).⁷ One notable exception is the dioxymethylene formation step from HCOOH^* (R32: $\text{HCOO}^* + \text{H}^* \rightarrow \text{H}_2\text{CO}_2^* + *$). Although it is a bond-making step, its activation energy barrier is 1.20 eV on Ni(110), 0.39 eV lower than that on Cu(111).³⁵ This offers an explanation for the dioxymethylene pathway being a viable methanol synthesis pathway on Ni(110), but not on Cu(111). We caution readers that the DFT values on Cu(111) were obtained using a different software package (DACAPO),^{35,75,76} and therefore small discrepancies should be expected. However, due to the generally large differences between the calculated reaction energetics on Ni(110) and Cu(111), the qualitative trends observed from this comparison should still be valid.

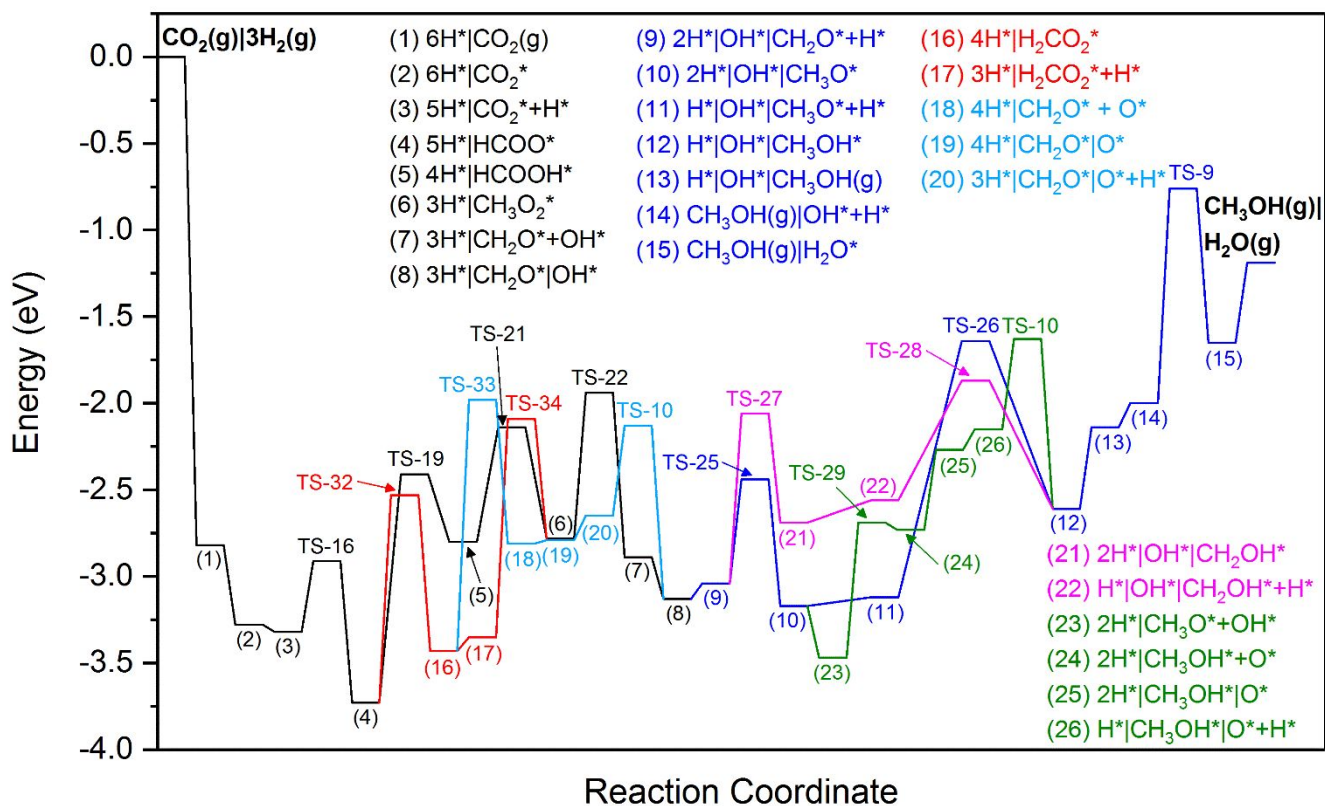


Figure 8. Potential energy diagram of methanol synthesis via CO₂ hydrogenation on Ni(110). The black and red lines denote the CH₂O* formation through the formic-acid- and dioxymethylene-mediated paths, respectively. The cyan line denotes the direct dissociation of hydroxymethoxy (CH₃O₂*) to CH₂O*. The purple line denotes the hydrogenation of CH₂O* to methanol via the CH₂OH* intermediate. The blue and green lines denote the hydrogenation of CH₂O* to methanol via the CH₃O* intermediate through the direct and OH-assisted paths, respectively. Intermediates are labeled as (1) – (26). Gas-phase and adsorbed species are denoted with (g) and *, respectively. Symbols + and | indicate co-adsorbed species and species at infinite separation, respectively. TS-*n* denotes the transition state of reaction R_{*n*} in Table 2. The total energy of gas-phase CO₂ and 3H₂ is set to zero.

3.4. Effect of CO: Promoter or reactant

Finally, we studied the effect of CO on methanol synthesis. The CO effect has been partially addressed above in the WGS reaction. We further considered the CO effect by examining CO-

assisted hydrogenation reaction steps using formyl (HCO^*) as the source for H. Additionally, we examined the hydrogenation of HCO^* , which eventually leads to the formation of methanol directly from CO. The relevant elementary steps are indicated as Steps R37 to R51 in Table 2.

(1) Formyl (HCO) formation. Our calculations show that on Ni(110), formyl HCO^* is 0.36 eV more stable than its isomer COH^* . Formyl formation via CO hydrogenation, i.e., $\text{CO}^* + \text{H}^* \rightarrow \text{HCO}^*$ (R37) is endothermic by 0.85 eV with an energy barrier of 1.06 eV. This indicates that the decomposition of HCO^* , i.e., the reverse reaction of R37, is very facile with a small energy barrier of 0.21 eV. The formation of COH^* via $\text{CO}^* + \text{H}^* \rightarrow \text{COH}^*$ (R38) has a much higher barrier of 1.45 eV and a reaction energy of 1.20 eV. Therefore, CO hydrogenation to HCO^* is favored over that to COH^* on Ni(110). HCO^* formation via formate decomposition, $\text{HCOO}^* \rightarrow \text{HCO}^* + \text{O}^*$ (R39), is highly activated with $E_a = 1.55$ eV and $\Delta E = 0.86$ eV. HCO^* can also be formed via formic acid decomposition, $\text{HCOOH}^* \rightarrow \text{HCO}^* + \text{OH}^*$ (R40). This step is exothermic by 0.42 eV with an energy barrier of 0.45 eV.

(2) Formyl (HCO) as an alternative H source. With HCO^* as an alternative source of hydrogen, O^* could be hydrogenated to OH^* in a concerted step (R45, $\text{O}^* + \text{HCO}^* \rightarrow \text{OH}^* + \text{CO}^*$). Interestingly, our calculations indicate that step R45 is not a concerted step but involves HCO^* decomposition (i.e., inverse of R37) first because HCO^* decomposition is facile (reverse of R37,

$E_a = 0.21$ eV, $\Delta E = -0.85$ eV) on Ni(110). This is also true for HCOO^* , HCOOH^* , and CH_2O^* hydrogenation using HCO^* as an alternative H^* source (R47-R50). Note that for formic acid hydrogenation to CH_3O_2^* , we found a concerted path with HCO^* as an alternative H source (R49). However, this concerted path has a higher barrier than the two-step sequential path with HCO^* decomposition as the first sub-step.

Remarkably, with HCO^* as an alternative H^* source, we found that CH_3O^* hydrogenation becomes easier: a concerted step exists: $\text{CH}_3\text{O}^* + \text{HCO}^* \rightarrow \text{CH}_3\text{OH}^* + \text{CO}^*$ (R51), which is exothermic by 0.45 eV and has an energy barrier of 0.90 eV. Plotted in Figure 9 is the potential energy diagram for methanol formation via CH_3O^* hydrogenation with HCO^* as the H^* source. During the reaction, CH_3O^* moves from the SB site to the neighboring top site, and the O atom of HCO^* rotates perpendicularly around C by breaking its O—Ni bonds. At the transition state (see inset of Figure 9), the two O—Ni bonds of CH_3O^* are broken; the distance between the H in CH_3O^* and the O in CH_3O^* is 1.92 Å; the H—C bond in CH_2O^* is elongated to 1.30 Å from 1.17 Å. After the transition state, the H—C bond in CH_2O^* is broken, and an H—O bond is formed with CH_3O^* . In the final state, CH_3OH^* binds to the top site, and CO^* binds to the SB site. Compared with Step R26, $\text{CH}_3\text{O}^* + \text{H}^* \rightarrow \text{CH}_3\text{OH}^*$, which is endothermic by 0.51 eV with an energy barrier of 1.48 eV, Step $\text{CH}_3\text{O}^* + \text{HCO}^* \rightarrow \text{CH}_3\text{OH}^* + \text{CO}^*$ (R51) is both

thermodynamically and kinetically more favorable. This indicates that in the presence of HCO^* , CH_3O^* hydrogenation to the product CH_3OH^* is significantly promoted.

Here, we focus on the discussion of HCO^* as an alternative H^* source instead of its isomer COH^* because: (1) on Ni(110), HCO^* is 0.36 eV more stable than COH^* (see discussion in Section 3.1); (2) from CO^* and H^* , the activation energy barrier for the formation of COH^* (R38: $\text{CO}^* + \text{H}^* \rightarrow \text{COH}^* + *$, $E_a = 1.45$ eV) is 0.39 eV higher than that for the formation of HCO^* (R37: $\text{CO}^* + \text{H}^* \rightarrow \text{HCO}^* + *$, $E_a = 1.06$ eV). It is also worth noting that because COH^* decomposition is facile (reverse of R38: $\text{CO}^* + \text{H}^* \rightarrow \text{COH}^* + *$, $E_a = 0.25$ eV, $\Delta E = -1.20$ eV), we were unable to observe any COH^* -facilitated hydrogenation as a concerted step. Instead, COH^* would be decomposed to CO^* and H^* first. For example, the reaction $\text{COH}^* + \text{O}^* \rightarrow \text{CO}^* + \text{OH}^*$ cannot occur as a single elementary step, but rather through a two-step process: $\text{COH}^* + * \rightarrow \text{CO}^* + \text{H}^*$ and $\text{O}^* + \text{H}^* \rightarrow \text{OH}^* + *$.

(3) Formyl (HCO) hydrogenation. HCO^* can be hydrogenated to either CH_2O^* (R41) or HCOH^* (R42). It turns out that the hydrogenation route to CH_2O^* is both thermodynamically and kinetically more favorable than the route to HCOH^* on Ni(110): the CH_2O^* route has a barrier of 0.52 eV and is slightly endothermic by 0.10 eV, while the HCOH^* route has a higher barrier of 0.90 eV and is endothermic by 0.38 eV. CH_2O^* can be further hydrogenated to the final product, methanol, through the reaction routes already discussed in Section 3.2. This is a possible route

for CO to participate directly in the formation of methanol. Our finding is in agreement with other recent DFT studies, where methanol formation from sequential hydrogenation of CO to HCO^* and CH_2O^* on Ni(110) was reported.^{77,78}

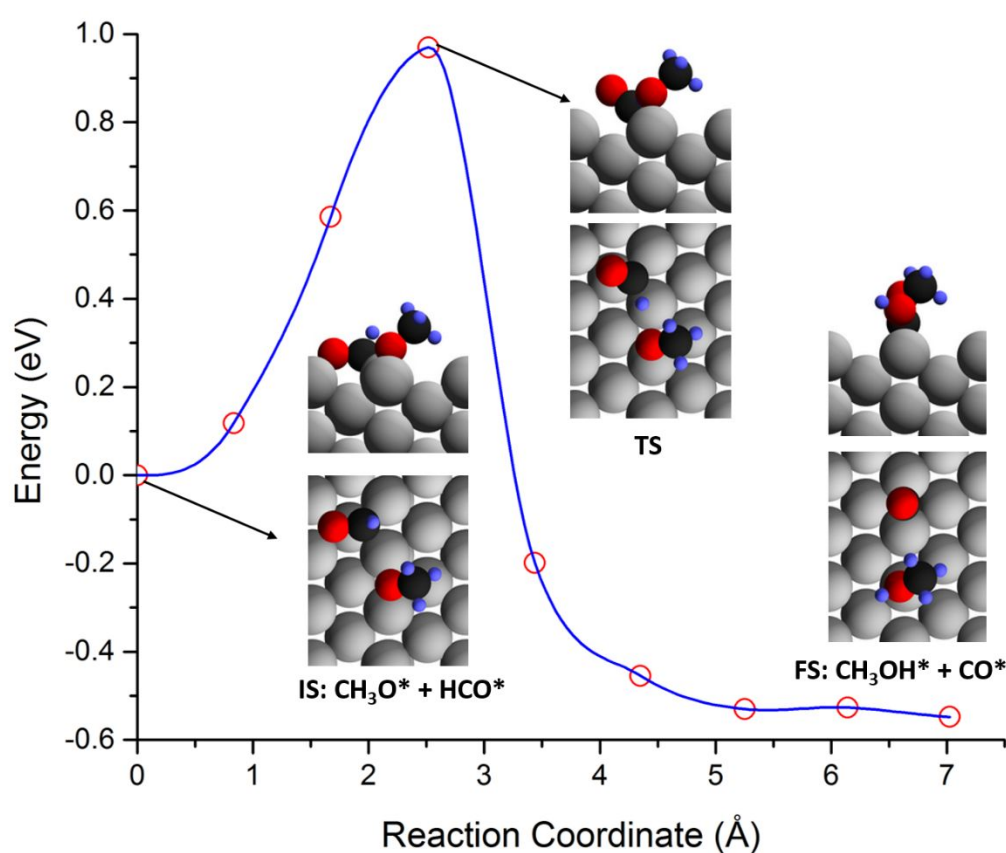


Figure 9. Potential energy diagram for methanol (CH_3OH) formation via methoxy (CH_3O) hydrogenation with HCO^* as the H source on Ni(110). Top and cross-section views of the atomic structure of the initial state (IS), transition-state (TS) and final state (FS) are shown in the insets. Blue, black, red, and gray spheres denote H, C, O, and Ni atoms, respectively.

3.5. Reaction Network for Methanol Synthesis

In Figure 10, we illustrated the reaction network for methanol synthesis on Ni(110) based on our DFT results. For CH_2O^* formation from CO_2 hydrogenation, the HCOOH^- and H_2CO_2^-

mediated paths co-exist. The H_2CO_2 -mediated path ($\text{CO}_2^* \rightarrow \text{HCOO}^* \rightarrow \text{H}_2\text{CO}_2^* \rightarrow \text{CH}_3\text{O}_2^* \rightarrow \text{CH}_2\text{O}^*$) is likely preferred due to the higher stability of H_2CO_2^* . Alternatively, CH_2O^* can be formed from the hydrogenation of CO ($\text{CO}^* \rightarrow \text{HCO}^* \rightarrow \text{CH}_2\text{O}^*$). The hydrogenation of CH_2O^* to the methanol product proceeds through either the CH_3O or the CH_2OH route. For the hydrogenation of CH_3O^* , a HCO-assisted path exists, which requires a lower energy barrier than the direct and the OH-assisted paths. We note that these results are based on DFT calculations only, and we have not considered experimental conditions such as temperature and partial pressure of $\text{CO}_2/\text{CO}/\text{H}_2$. Additional microkinetic modeling by considering feed composition and reaction conditions would provide further mechanistic insights into methanol synthesis on Ni(110). The microkinetic model could also be extended to include elementary steps in the CO/ CO_2 methanation mechanism; such a model would enable the identification of reaction conditions under which the selectivity to methanol over methane is maximized on Ni catalysts. Another potential area for exploration is the possibility of adsorbate-induced surface reconstruction on Ni(110) under methanol synthesis conditions. Past scanning-tunneling microscopy (STM) studies have demonstrated H-induced reconstructions on Ni(110) under ultrahigh vacuum conditions.^{79,80} While our current study on the pristine Ni(110) surface should serve as a good initial estimate for the reaction energetics, *in-situ* studies, from both experiments and theory, for the catalyst surface

structure could provide valuable insights on the nature of active sites in the Ni-catalyzed methanol synthesis reaction.

A key distinction between the methanol synthesis pathways on Ni(110) and Cu(111) is the presence of the H_2CO_2 -mediated pathway on Ni(110). The adsorption properties and reactivities of the H_2CO_2^* intermediate may serve as guiding criteria for improving methanol synthesis catalysts. It should be noted that the two key elementary steps involved in the H_2CO_2 -mediated pathway (R32: $\text{HCOO}^* + \text{H}^* \rightarrow \text{H}_2\text{CO}_2^* + *$ and R34: $\text{H}_2\text{CO}_2^* + \text{H}^* \rightarrow \text{CH}_3\text{O}_2^* + *$) are still notably activated (with $E_a = 1.20$ eV and 1.34 eV for R32 and R34, respectively) on Ni(110). Using the DFT results on Ni(110) as benchmark, one could design and engineer catalytic surfaces with sites that exhibit lower activation energy barriers for these elementary steps, which may eventually lead to the H_2CO_2 -mediated pathway being the clearly dominant pathway over the HCOOH -mediated counterpart and potentially higher overall activity toward methanol synthesis.

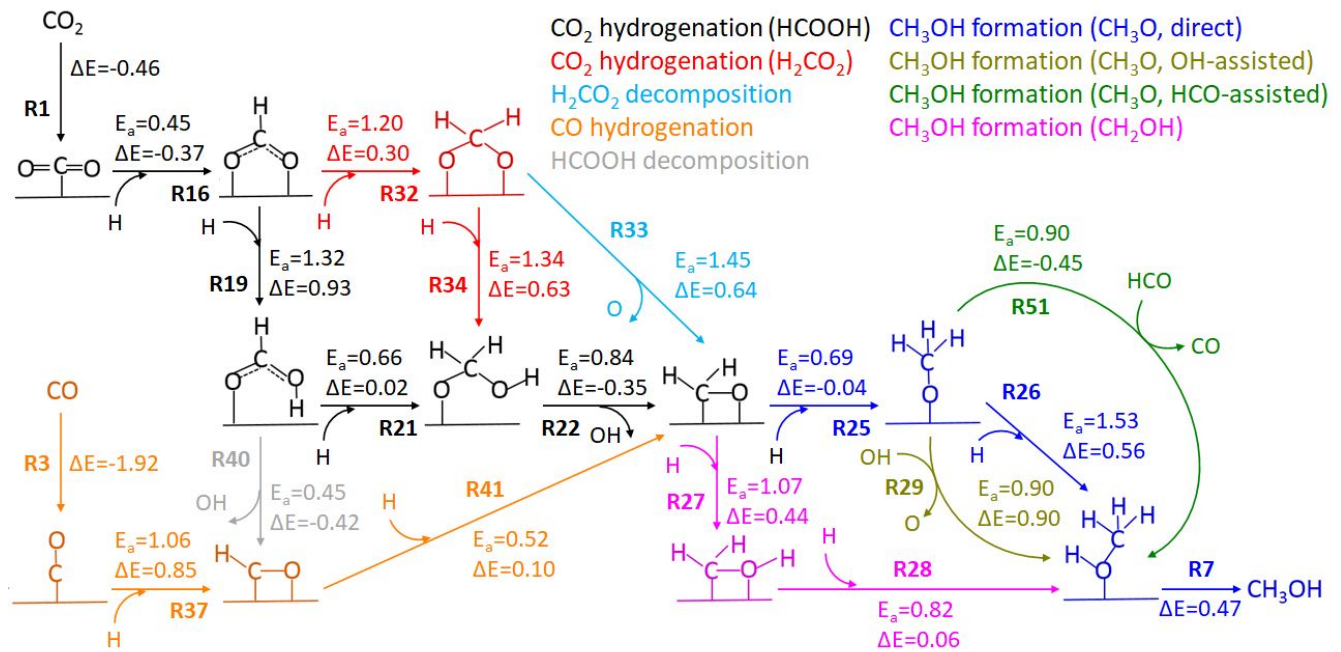


Figure 10. DFT-derived reaction network for methanol synthesis on Ni(110) derived by DFT. The reaction energies (ΔE) and the activation energy barriers (E_a) for all the elementary steps are given in eV. The label R*n* refers to the elementary steps given in Table 2.

4. Conclusions

In summary, we presented a planewave DFT-PW91 study of methanol synthesis, the WGS reaction, and formic acid formation on Ni(110). For the WGS reaction on Ni(110), we found that the redox mechanism is favored over the carboxyl-mediated mechanism, mainly because the formation of carboxyl from CO^* and OH^* is extremely difficult on Ni(110). This is in contrast to the WGS reaction on Cu(111) where the carboxyl-mediated mechanism dominates. For formic acid formation from CO_2 hydrogenation, the formate pathway is favored over the carboxyl pathway on Ni(110). For methanol synthesis through CO_2 and CO hydrogenation on Ni(110), our results showed that the formic-acid- and dioxymethylene-mediated pathways coexist, in contrast to the methanol synthesis on Cu(111) where the formic-acid-mediated pathway dominates. We also found that on Ni(110), the hydrogenation step of CH_2O^* to CH_3O^* and that to CH_2OH^* compete with each other. This is different from the situation on Cu(111), where the CH_3O^* pathway dominates. Similar to the case on Cu(111), CH_3O^* hydrogenation to CH_3OH^* is the likely rate-determining step along the CH_3O pathway on Ni(110). Remarkably, on Ni(110), CH_3O^* hydrogenation can be facilitated by the presence of HCO^* (as a source of Hydrogen), demonstrating the promotional effect of CO. Note that besides acting as a promoter, CO also participates in methanol synthesis directly as CO is hydrogenated to HCO^* which is further

hydrogenated to CH_2O^* , and eventually to CH_3OH^* (through CH_3O^* or CH_2OH^*). Our results demonstrate the distinct behavior of Ni(110) in methanol synthesis as compared to the conventional Cu-based catalysts.

Conflicts of Interest: The authors declare no conflict of interest.

Acknowledgements. This work was supported by the U.S. Department of Energy – Basic Energy Sciences (DOE-BES), Office of Chemical Sciences, Catalysis Science Program (Grant DE-FG02-05ER15731). V.-A. G. acknowledges support by the U.S. Department of Energy, Office of Science, Office of Basic Energy Sciences, Division of Chemical Sciences, Geosciences, and Biosciences. The computational work was performed in part by using supercomputing resources from the following institutions: EMSL, a DOE Office of Science User Facility at Pacific Northwest National Laboratory (PNNL); and the National Energy Research Scientific Computing Center (NERSC), a DOE Office of Science User Facility located at Lawrence Berkeley National Laboratory and operated under Contract DE-AC02-05CH11231. PNNL is operated by Battelle for DOE under Contract DE-AC05-76RL01830.

References:

- (1) W. Leitner, *Angew. Chem.-Int. Edit.* 1995, **34**, 2207.
- (2) P. G. Jessop, T. Ikariya, R. Noyori, *Chem. Rev.* 1995, **95**, 259.
- (3) G. A. Olah, A. Goepfert, G. K. S. Prakash, *Beyond Oil and Gas: The Methanol Economy*, Wiley-VCH Verlag GmbH & Co. KGaA: Weinheim, 2006.
- (4) A. Hamnett, *Catalysis Today* 1997, **38**, 445.
- (5) S. Wasmus, A. Kuver, *J. Electroanal. Chem.* 1999, **461**, 14.
- (6) S. Lee, *Methanol Synthesis Technology*, CRC Press: Boca Raton, FL, 1989.
- (7) A. A. Gokhale, J. A. Dumesic, M. Mavrikakis, *J. Am. Chem. Soc.* 2008, **130**, 1402.

- (8) L. C. Grabow, A. A. Gokhale, S. T. Evans, J. A. Dumesic, M. Mavrikakis, *J. Phys. Chem. C* 2008, **112**, 4608.
- (9) G. Natta, In *Catalysis*; Emmett, P. H., Ed.; Reinhold: New York, 1955, p 349.
- (10) K. Klier, *Advances in Catalysis* 1982, **31**, 243.
- (11) G. C. Chinchin, P. J. Denny, D. G. Parker, M. S. Spencer, D. A. Whan, *Appl. Catal.* 1987, **30**, 333.
- (12) K. C. Waugh, *Catal. Today* 1992, **15**, 51.
- (13) J. Szanyi, D. W. Goodman, *Catal. Lett.* 1991, **10**, 383.
- (14) P. B. Rasmussen, P. M. Holmblad, T. Askgaard, C. V. Ovesen, P. Stoltze, J. K. Nørskov, I. Chorkendorff, *Catal. Lett.* 1994, **26**, 373.
- (15) P. B. Rasmussen, M. Kazuta, I. Chorkendorff, *Surf. Sci.* 1994, **318**, 267.
- (16) J. Yoshihara, S. C. Parker, A. Schafer, C. T. Campbell, *Catal. Lett.* 1995, **31**, 313.
- (17) J. Yoshihara, C. T. Campbell, *J. of Catal.* 1996, **161**, 776.
- (18) J. B. Hassen, P. E. H. Nielsen, In *Handbook of Heterogeneous Catalysis*; G. Ertl, H. Knozinger, F. Schuth, J. Weitkamp, Eds.; Wiley-VCH Verlag GmbH & Co. KGaA: Weinheim: 2008.
- (19) M. Behrens, F. Studt, I. Kasatkin, S. Kühl, M. Hävecker, F. Abild-Pedersen, S. Zander, F. Girgsdies, P. Kurr, B. -L. Kniep, M. Tovar, R. W. Fischer, J. K. Nørskov, R. Schlögl, *Science* 2012, **336**, 89.
- (20) Y.-F. Zhao, Y. Yang, C. Mims, C. H. F. Peden, J. Li, D. Mei, *J. Catal.* 2011, **281**, 199.
- (21) S. Natesakhawat, J. W. Lekse, J. P. Baltrus, P. R. Ohodnicki, B. H. Howard, X. Deng, C. Matranga, *ACS Catal.* 2012, **2**, 1667.
- (22) Y. Yang, C. A. Mims, D. H. Mei, C. H. F. Peden, C. T. Campbell, *J. Catal.* 2013, **298**, 10.
- (23) F. Studt, M. Behrens, E. L. Kunkes, N. Thomas, S. Zander, A. Tarasov, J. Schumann, E. Frei, J. B. Varley, F. Abild-Pedersen, J. K. Nørskov, R. Schlögl, *ChemCatChem* 2015, **7**, 1105.
- (24) W. Janse van Rensburg, M. A. Petersen, M. S. Datt, J. -A. van den Berg, P. van Helden, *Catal. Letters* 2015, **145**, 559.
- (25) S. Kuld, M. Thorhauge, H. Falsig, C. F. Elkjær, S. Helveg, I. Chorkendorff, J. Sehested, *Science* 2016, **352**, 969.
- (26) S. Kattel, P. J. Ramírez, J. G. Chen, J. A. Rodriguez, P. Liu, *Science* 2017, **355**, 1296.

- (27) B. An, J. Zhang, K. Cheng, P. Ji, C. Wang, W. Lin, *J. Amer. Chem. Soc.* 2017, **139**, 3834.
- (28) K. Larmier, W. -C. Liao, S. Tada, E. Lam, R. Verel, A. Bansode, A. Urakawa, A. Comas-Vives, C. Copéret, *Angew. Chem. Int. Ed.* 2017, **56**, 2318.
- (29) S. Dang, H. Yang, P. Gao, H. Wang, X. Li, W. Wei, Y. Sun, *Catal. Today* 2019, **330**, 61.
- (30) J. Zhong, X. Yang, Z. Wu, B. Liang, Y. Huang, T. Zhang, *Chem. Soc. Rev.* 2020, **49**, 1385.
- (31) V. D. B. C. Dasireddy and B. Likozar, *Renew. Energy*, 2019, **140**, 452–460.
- (32) S. Dang, H. Yang, P. Gao, H. Wang, X. Li, W. Wei and Y. Sun, *Catal. Today*, 2019, **330**, 61–75.
- (33) J. Zhong, X. Yang, Z. Wu, B. Liang, Y. Huang and T. Zhang, *Chem. Soc. Rev.*, 2020, **49**, 1385–1413.
- (34) S. Sarkar, S. S. Sumukh, K. Roy, N. Kamboj, T. Purkait, M. Das and R. S. Dey, *J. Colloid Interface Sci.*, 2020, **558**, 182–189.
- (35) L. C. Grabow, M. Mavrikakis, *ACS Catal.* 2011, **1**, 365.
- (36) J. Nerlov, I. Chorkendorff, *J. Catal.* 1999, **181**, 271.
- (37) J. Nerlov, S. Sckerl, J. Wambach, I. Chorkendorff, *Appl. Catal. A* 2000, **191**, 97.
- (38) A. I. Alharthi, I. U. Din and M. A. Alotaibi, *Russ. J. Phys. Chem. A*, 2020, **94**, 2563–2568.
- (39) Q. Tan, Z. Shi and D. Wu, *Ind. Eng. Chem. Res.*, 2018, **57**, 10148–10158.
- (40) P. Sabatier and J. B. Senderens, *Comptes Rendus l'Académie des Sci. Paris*, 1902, **134**, 514–516.
- (41) G. Weatherbee, *J. Catal.*, 1982, **77**, 460–472.
- (42) R. Mutschler, E. Moiola, W. Luo, N. Gallandat and A. Züttel, *J. Catal.*, 2018, **366**, 139–149.
- (43) S. -G. Wang, D. -B. Gao, Y. -W. Li, J. Wang, H. J. Jiao, *Phys. Chem. B* 2005, **109**, 18956.
- (44) B. Bartos, H. -J. Freund, H. Kühlenbeck, M. Neumann, H. Lindner, K. Müller, *Surf. Sci.* 1987, **179**, 59.
- (45) X. Ding, L. De Rogatis, E. Vesselli, A. Baraldi, G. Comelli, R. Rosei, L. Savio, L. Vattuone, M. Rocca, P. Fornasiero, F. Ancilotto, A. Baldereschi, M. Peressi, *Phys. Rev. B* 2007, **76**, 195425.

- (46) E. Vesselli, L. De Rogatis, X. Ding, A. Baraldi, L. Savio, L. Vattuone, M. Rocca, P. Fornasiero, M. Peressi, A. Baldereschi, R. Rosei, G. Comelli, *J. Am. Chem. Soc.* 2008, **130**, 11417.
- (47) C. Vogt, E. Groeneveld, G. Kamsma, M. Nachtegaal, L. Lu, C. J. Kiely, P. H. Berben, F. Meirer and B. M. Weckhuysen, *Nat. Catal.*, 2018, **1**, 127–134.
- (48) X. Jia, X. Zhang, N. Rui, X. Hu and C. Liu, *Appl. Catal. B Environ.*, 2019, **244**, 159–169.
- (49) W. Li, X. Nie, X. Jiang, A. Zhang, F. Ding, M. Liu, Z. Liu, X. Guo and C. Song, *Appl. Catal. B Environ.*, 2018, **220**, 397–408.
- (50) C. Italiano, J. Llorca, L. Pino, M. Ferraro, V. Antonucci and A. Vita, *Appl. Catal. B Environ.*, 2020, **264**, 118494.
- (51) G. Kresse, J. Furthmuller, *Phys. Rev. B* 1996, **54**, 11169.
- (52) G. Kresse, J. Furthmuller, *Comput. Mater. Sci.* 1996, **6**, 15.
- (53) P. E. Blochl, *Phys. Rev. B* 1994, **50**, 17953.
- (54) G. Kresse, D. Joubert, *Phys. Rev. B* 1999, **59**, 1758.
- (55) J. P. Perdew, Y. Wang, Y. *Phys. Rev. B* 1992, **45**, 13244.
- (56) J. Neugebauer, M. Scheffler, *Phys. Rev. B* 1992, **46**, 16067.
- (57) L. Bengtsson, *Phys. Rev. B* 1999, **59**, 12301.
- (58) H. J. Monkhorst, J. D. Pack, *Phys. Rev. B* 1976, **13**, 5188.
- (59) G. Henkelman, B. P. Uberuaga, H. Jonsson, H. *J. Chem. Phys.* 2000, **113**, 9901.
- (60) *CRC Handbook of Chemistry and Physics, 76th ed.*; CRC Press: New York, 1996.
- (61) B. E. Wilson, J. C. Decius, P. C. Cross, *Molecular Vibrations*; McGraw-Hill: New York, 1955.
- (62) G. W. Peng, S. J. Sibener, G. C. Schatz, S. T. Ceyer, M. Mavrikakis, *J. Phys. Chem. C* 2012, **116**, 3001.
- (63) G. W. Peng, L. P. Merte, J. Knudsen, R. T. Vang, E. Laegsgaard, F. Besenbacher, M. Mavrikakis, *J. Phys. Chem. C* 2010, **114**, 21579.
- (64) M. P. Andersson, F. Abild-Pedersen, I. N. Remediakis, T. Bligaard, G. Jones, J. Engbæk, O. Lytken, S. Horch, J. H. Nielsen and J. Sehested, *J. Catal.*, 2008, **255**, 6–19.
- (65) I. N. Remediakis, F. Abild-Pedersen and J. K. Nørskov, *J. Phys. Chem. B*, 2004, **108**, 14535–14540.
- (66) G. W. Peng, S. J. Sibener, G. C. Schatz, M. Mavrikakis, *Surf. Sci.* 2012, **606**, 1050.

- (67) N. Schumacher, K. Andersson, L. C. Grabow, M. Mavrikakis, J. Nerlov, Chorkendorff, I. *Surf. Sci.* 2008, **602**, 702.
- (68) K. Waugh, *Solid State Ionics* 2004, **168**, 327.
- (69) N. C. Nelson, M.-T. Nguyen, V.-A. Glezakou, R. Rousseau and J. Szanyi, *Nat. Catal.*, 2019, **2**, 916.
- (70) J. F. Edwards, G. L. Schrader, *J. Catal.* 1985, **94**, 175.
- (71) I. A. Fisher, A. T. Bell, *J. Catal.* 1997, **172**, 222.
- (72) B. A. Sexton, A. E. Hughes, N. R. Avery, *Surf. Sci.* 1985, **155**, 366.
- (73) G. Busca, J. Lamotte, J. C. Lavalley, V. Lorenzelli, V. *J. Am. Chem. Soc.* 1987, **109**, 5197.
- (74) J. R. B. Gomes, J. Gomes, *Surf. Sci.* 2000, **446**, 283.
- (75) B. Hammer, L. B. Hansen, J. K. Nørskov, *Phys. Rev. B* 1999, **59**, 7413.
- (76) J. Greeley, J. K. Nørskov, M. Mavrikakis, *Annu. Rev. Phys. Chem.* 2002, **53**, 319.
- (77) J. L. C. Fajín, J. R. B. Gomes, M. N. D. S. Cordeiro, *J. Phys. Chem. C* 2015, **119**, 16537.
- (78) A. P. Ashwell, W. Lin, M. S. Hofman, Y. Yang, M. A. Ratner, B. E. Koel, G. C. Schatz, *J. Am. Chem. Soc.* 2017, **139**, 17582.
- (79) Y. Uehara and S. Ushioda, *Surf. Sci.*, 2007, **601**, 5643–5648.
- (80) L. P. Nielsen, F. Besenbacher, E. Laegsgaard and I. Stensgaard, *Phys. Rev. B*, 1991, **44**, 13156(R).